

Collisional mechanism for GRB emission

Andrei M. Beloborodov^{*}

*Physics Department and Columbia Astrophysics Laboratory, Columbia University, 538 West 120th Street New York, NY 10027;
amb@phys.columbia.edu*

11 November 2018

ABSTRACT

Nuclear and Coulomb collisions in GRB jets create a hot e^\pm plasma. This collisional heating starts when the jet is still opaque and extends to the transparent region. The e^\pm plasma radiates its energy. As a result, a large fraction of the jet energy is converted to escaping radiation with a well-defined spectrum. The process is simulated in detail using the known rates of collisions and accurate calculations of radiative transfer in the expanding jet. The result reproduces the spectra of observed GRBs that typically peak near 1 MeV and extend to much higher energies with a photon index $\beta \sim -2.5$. This suggests that collisional heating may be the main mechanism for GRB emission.

Key words: gamma-rays: bursts, theory — plasmas — radiation mechanisms: thermal, non-thermal — radiative transfer — relativity — scattering.

1 INTRODUCTION

Cosmological gamma-ray bursts (GRBs) are associated with ultra-relativistic jets from short-lived powerful sources such as hyper-accreting, just-born black holes. The jet starts as an opaque blackbody fireball that accelerates, expands and releases its thermal radiation at the photospheric radius R_* . One may expect a quasi-blackbody spectrum from such jets (Paczynski 1986; Goodman 1986), similar to the relict radiation from the big bang. However, the simple blackbody model is inconsistent with observations (e.g. Preece et al. 2000). It is clear that some form of heating operates in the jet and changes its radiation from blackbody. Heating may occur at radii $r < R_*$ and change the photospheric radiation via Comptonization. It may also occur at radii $r > R_*$ and generate nonthermal synchrotron emission.

Two heating mechanisms are usually considered in GRB jets: internal shocks and dissipation of magnetic energy. The details of both mechanisms are uncertain as they depend on complicated *collisionless* processes in the plasma. A long-standing problem is the radiative efficiency of these processes.

Recent observations by *Fermi* telescope provided new data in a broad spectral range from 8 keV to ~ 100 GeV. The data confirm the previous BATSE result that the prompt GRB spectrum typically peaks near MeV (Preece et al. 2000). The typical spectrum is approximately described by the Band function (a smoothly broken power law), which extends to high-energy bands with a photon index $\beta \sim -2.5$. The prompt GRB radiation is highly variable on timescales as short as millisecond, suggesting a small radius of emission, possibly comparable to the photospheric radius R_* .¹

The spectrum of GRB emission at very high energies $E \gtrsim 1$ GeV remains so far uncertain. Multi-GeV photons overlapping the prompt MeV radiation have been detected in about 5 per cent of GRBs, however they may be produced by a distinct source at large radii, e.g. by the blast wave from the explosion. The distinct source is visible in several GeV-emitting bursts (e.g. Abdo et al. 2009b; Ryde et al. 2010) and likely present in all of them, obscuring the behavior of the prompt Band spectrum at high energies (cf. the debate over GRB 080916C: Abdo et al. 2009a; Kumar & Barniol Duran 2009; Ghisellini et al. 2009).

The standard theory (e.g. Paczyński 1990) predicts that jets with $\Gamma \sim 10^3$ must produce bright photospheric emission. Observational search for this emission usually assumed that it has a quasi-thermal spectrum (e.g. Ryde 2005). It was argued that the absence of the photospheric emission component would imply that the jet is magnetically dominated and cold, with negligible initial thermal energy (e.g. Daigne & Mochkovitch 2002; Zhang & Pe'er 2009).

The main finding of the present paper is that the Band-type spectrum naturally forms in GRB jets as a result of *collisional* heating. Most of radiation produced by this mechanism is emitted near the photosphere R_* and therefore it may be called photospheric to a first approximation. Our result supports the view that photospheric emission is not a rare quasi-thermal component; instead, it is the main Band component of GRB emission that is routinely observed in all bursts.

This paper considers the standard model of a baryonic jet with comparable numbers of neutrons and protons (our model would not work for jets that are completely dominated by magnetic field, with negligible baryonic loading). Before becoming transparent to

^{*} Also at Astro-Space Center of Lebedev Physical Institute, Profsojuznaja 84/32, Moscow 117810, Russia

¹ Recent suggestions that the prompt γ -ray emission must come from a

large radius $r \gg R_*$ (e.g. Racusin et al. 2008; Abdo et al. 2009a) are based on incorrect assumptions (see Section 6.1).

radiation, the jet evolves to the two-fluid or ‘compound’ state: a plasma with bulk Lorentz factor Γ embeds a neutron flow with Lorentz factor $\Gamma_n < \Gamma$ (Derishev, Kocharovsky & Kocharovsky 1999a; Bahcall & Mészáros 2000; Fuller, Pruet & Abazajian 2000; Mészáros & Rees 2000; Rossi, Beloborodov & Rees 2006; Koers & Giannios 2007). Regardless the details of their formation, compound jets with $\Gamma_n \ll \Gamma$ have a robust feature: nuclear collisions between the neutron and proton fluids continually create multiple e^\pm with energies $\sim m_\pi c^2 \approx 140$ MeV. Their energy is immediately converted to radiation before e^\pm join the thermalized plasma. Nuclear collisions also heat the proton component of the jet, and protons gradually drain their energy into thermalized e^\pm plasma via Coulomb collisions.

Similarly to internal shocks, collisional heating taps the kinetic energy of internal motions in the jet — the streaming of plasma through the neutron component with a relative Lorentz factor $\Gamma_{\text{rel}} = \frac{1}{2}(\Gamma/\Gamma_n + \Gamma_n/\Gamma)$. In contrast to internal shocks, the heating is not confined to a shock front. It operates in volume.

Several works previously proposed that some sort of volume heating shapes the spectrum of GRB emission (e.g. Thompson 1994; Ghisellini & Celotti 1999; Stern & Poutanen 2004; Rees & Mészáros 2005; Pe’er, Mészáros & Rees 2005; Giannios & Spruit 2007; Ioka et al. 2007; Asano & Terasawa 2009). The models assumed some form of collisionless dissipation, which is difficult to calculate from first principles. In this context, two special features of our model should be noted:

(i) The collisional heating is robust, and its history in the expanding jet is well defined. The rate of collisions determines the radial dependence of the heating rate $\dot{Q} \propto r^{-2}$.

(ii) The collisional heating injects energy into e^\pm via two branches with comparable heating rates:

(a) Nuclear collisions maintain a continual e^\pm cascade in the jet.

(b) Coulomb collisions in the two-temperature plasma² continually transfer energy from protons to thermalized e^\pm .

Branch (a) is important because it loads the jet with a large number of e^\pm pairs and determines the photospheric radius of the burst. On the other hand, it will be shown that branch (b) plays an important role in the formation of the GRB spectrum. The radiation emerging from a collisionally heated jet has a well defined spectrum, which can be calculated numerically. This radiative transfer problem is solved in this paper using a Monte-Carlo code that tracks the evolution of photons and e^\pm in the heated and expanding plasma flow.

The paper is organized as follows. Section 2 gives a compact summary of the simplest model of GRB jets with no internal dissipation. Such jets passively cool down as they expand, and eventually emit thermal radiation whose spectrum cuts off exponentially at \sim MeV. It is inconsistent with the observed GRB spectra. We use the model of a passively cooling jet as a benchmark and a first test problem for our radiative transfer code.

Section 3 describes neutron-loaded jets and formation of compound flows with $\Gamma_n < \Gamma$. Section 4 describes the collisional radiative mechanism operating in compound flows. Section 5 presents the radiation spectrum received by distant observers. The results are discussed in Section 6. Section 6 also discusses the possibility of additional emission that may be generated by neutron decay.

GRB outflows are believed to be beamed and therefore called

‘jets’ throughout this paper. However, the results apply equally well to spherically symmetric outflows. As long as the opening angle of the explosion exceeds $1/\Gamma$, the jet near the axis is causally disconnected from its edge, and its dynamics is the same as that of a spherically symmetric flow.

2 THERMAL EMISSION FROM PASSIVELY COOLING JETS

We focus in this paper on jets that are accelerated by thermal (radiation) pressure, with a subdominant magnetic field. This standard model is briefly summarized below (see e.g. Paczyński 1990).

At small radii r , the GRB jet is in thermodynamic equilibrium and its luminosity is carried mainly by radiation $L \approx (4/3)caT^4\Gamma^2 4\pi r^2$ (hereafter we use the isotropic equivalent of luminosity, which would be produced by a spherically symmetric outflow of the same density and temperature). As the jet expands adiabatically, the ratio of photon and baryon number densities n_γ/n remains constant, i.e. effectively the photon number is conserved (similar to the cosmological big bang). The jet accelerates until the radiation energy density $U_\gamma = aT^4$ decreases below the rest-mass density $nm_p c^2$. Then its Lorentz factor saturates at the asymptotic Γ . We will denote the characteristic saturation radius by R_s . For a radially expanding jet,

$$R_s \approx \Gamma r_0, \quad (1)$$

where r_0 is the radius at the base of the jet, at the beginning of its acceleration. The photon-to-baryon ratio in the jet is given by

$$\frac{n_\gamma}{n} \approx 240 \Gamma r_{0,7}^{1/2} L_{52}^{-1/4}, \quad (2)$$

and the jet energy *per photon* is

$$\bar{E}_0 \approx \frac{\Gamma m_p c^2 n}{n_\gamma} \approx 4 r_{0,7}^{-1/2} L_{52}^{1/4} \text{ MeV}. \quad (3)$$

If no heat is generated by any dissipative processes, the thermal radiation trapped in the opaque flow continues to cool adiabatically at $r > R_s$ until it is released at the photosphere R_* . Between R_s and R_* , the radiation temperature decreases as $n^{\hat{\gamma}-1}$ where $\hat{\gamma} = 4/3$ is the adiabatic index of radiation, which gives $\bar{E} \propto r^{-2/3}$. The plasma has a small heat capacity (for $n \ll n_\gamma$) and simply tracks the radiation temperature. Electrons are thermally coupled to radiation via Compton scattering, and ions maintain thermal equilibrium with electrons via Coulomb collisions at a common low temperature $kT \lesssim 1$ keV in the rest frame of the jet.

The optical depth of the jet is given by

$$\tau_T = \frac{n\sigma_T r}{\Gamma} = \frac{L\sigma_T}{4\pi r m_p c^3 \Gamma^3} \approx r_{10}^{-1} L_{52} \Gamma_3^{-3}, \quad (4)$$

where $\sigma_T = 6.65 \times 10^{-25} \text{ cm}^2$ is Thomson cross section and $L = 4\pi r^2 \Gamma^2 n m_p c^3$ is the isotropic equivalent of the kinetic luminosity of the jet (it approximately equals the total luminosity at $r > R_s$). The photosphere radius $R_* \approx 10^{10} L_{52} \Gamma_3^{-3} \text{ cm}$ is larger than R_s for $\Gamma < 10^3 L_{52}^{1/4} r_{0,7}^{-1/4}$. The radiation luminosity released at the photosphere is $L_\gamma \approx (R_*/R_s)^{-2/3} L$, and the mean energy of the escaping photons is given by

$$\bar{E}(R_*) \sim \left(\frac{R_*}{R_s}\right)^{-2/3} \bar{E}_0 \approx 4 \Gamma_3^{8/3} L_{52}^{-5/12} r_{0,7}^{1/6} \text{ MeV}. \quad (5)$$

The thermal radiation creates a bright burst with MeV peak if $\Gamma \sim 10^3$. The burst is weak for slower flows: $L_\gamma \propto \Gamma^{8/3}$.

We have calculated the radiation spectrum emerging from the

² The thermalized e^\pm are Compton-cooled and kept at a temperature much lower than the proton temperature (see Section 4.4).

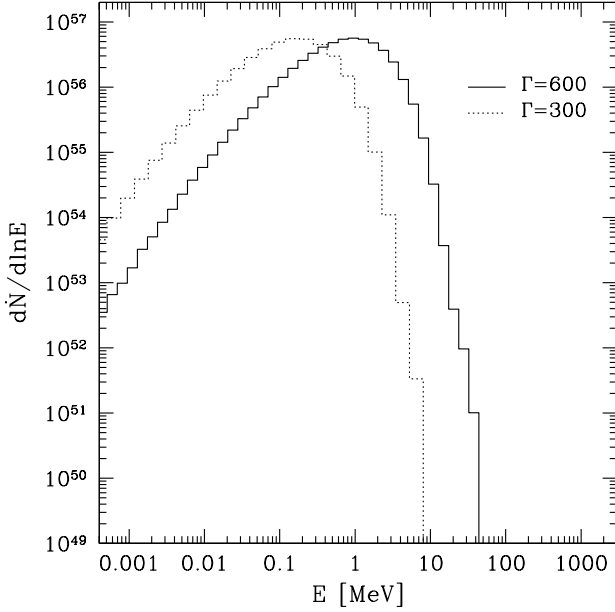


Figure 1. Photon spectrum emitted by a passively cooling jet to distant observers. The jet has kinetic luminosity $L = 10^{52}$ erg/s (isotropic equivalent) and initial size $r_0 = 10^7$ cm. It implies the total number flux of photons (isotropic equivalent) $\dot{N} = 1.6 \times 10^{57} \text{ s}^{-1}$. The photon spectrum has been calculated using the Monte-Carlo radiative transfer code. Two cases are shown: jets with asymptotic Lorentz factors $\Gamma = 600$ and 300 . The slopes of the spectra near 10 keV are close to 1.4, which corresponds to photon index $\alpha = 0.4$. The spectrum cuts off exponentially at $E > E_{\text{peak}} \sim 1$ MeV.

passively cooling jet using the Monte-Carlo code described in Appendix B. The scattering of the initial Planck spectrum was followed until the jet expanded to complete transparency. The spectrum of radiation received by distant observers is shown in Figure 1 for two example models. In qualitative agreement with the above estimates, the jet with $\Gamma = 600$ produces a bright GRB, whose spectrum peaks near MeV and cuts off exponentially. Two details are worth mentioning:

(i) Radiation emitted by passively cooling jets is not Planckian. Observer sees different parts of the photosphere at different angles, with different Doppler shifts. As a result, the low-energy slope of observed spectrum is softer than the Rayleigh-Jeans $\alpha = 1$ (photon index). Isotropic emission in the jet frame would produce $\alpha = 0$, and the exact α is controlled by the photon angular distribution near photosphere (e.g. $\alpha \approx 0.4$ near 10 keV in Fig. 1).

(ii) The standard description of adiabatic cooling predicts that radiation from a source at optical depth τ_T is cooled by the factor $A(\tau_T) = \tau_T^{-2/3}$ by the time the jet expands to its photospheric radius. The detailed transfer calculations give larger A . For example, $A(8) = 0.58$ instead of $8^{-2/3} = 0.25$ and $A(20) = 0.39$ instead of $20^{-2/3} \approx 0.14$. The scaling $A \propto \tau_T^{-2/3}$ is maintained at large $\tau_T > 10$.

The radiative transfer simulations illustrate and refine the standard fireball picture. They show that thermal radiation emitted by a passively cooling jet with $\Gamma > 500$ peaks at $E_{\text{peak}} \sim 1$ MeV and carries away a significant fraction ϵ of the jet energy (e.g. $\epsilon \approx 1/4$ for the model with $\Gamma = 600$ in Fig. 1). However, its spectrum cuts off exponentially at $E > E_{\text{peak}}$. Therefore, the model fails

to explain the observed GRBs, whose spectra extend to energies $E \gg E_{\text{peak}}$.

3 NEUTRON COMPONENT AND COMPOUND FLOWS

The picture described in Section 2 is incomplete, because it neglects the neutron component of the jet. In any plausible scenario of the GRB trigger, the central engine is dense, hot and neutron rich (Derishev, Kocharovsky & Kocharovsky 1999b; Beloborodov 2003). In particular, accretion-disc models for GRBs predict a high neutron fraction (see Beloborodov 2008 for a review). The neutron-rich matter is expected to enter the relativistic jet (although the details of this process may vary, see e.g. Levinson & Eichler 2003; Metzger, Thompson & Quataert 2008), and the neutron-proton jet initially accelerates as a single fluid where n and p are coupled by frequent nuclear collisions.

Neutrons and protons tend to combine into helium where the jet temperature drops to 140 keV. This process, however, competes with rapid expansion and is marginally successful. Collimation of the jet generally helps nucleosynthesis because it slows down expansion (cf. Fig. 4 and 5 in Beloborodov 2003). However, even in cases where helium production is complete, some neutrons survive in jets with a neutron excess, as helium production consumes equal numbers of n and p . In addition, free neutrons are produced by spallation of α -particles at larger radii where the jet is heated.

The expansion of neutron-loaded jets generally leads to the formation of a *compound flow*: a slower neutron component with Lorentz factor Γ_n is embedded in a faster proton flow with Lorentz factor $\Gamma > \Gamma_n$. The compound flow develops at the characteristic radius R_n where the timescale for n - p collisions becomes longer than the jet expansion time.

In particular, in jets that accelerate to $\Gamma > \Gamma_{\text{crit}} \approx 400 L_{52}^{1/4} r_{0,7}^{-1/4}$ neutrons do not develop the full Lorentz factor — their Γ_n saturates at a smaller value (Derishev et al. 1999a; Fuller et al. 2000). For example, a baryonic flow accelerated to $\Gamma = 10^3$ can contain neutrons with $\Gamma_n \sim 10^2$. In spite of the significant difference in Lorentz factors, the two components move together without any separation for a long time, because their velocities relative to the central engine are almost equal (the velocities practically equal c).

Even in jets with $\Gamma < \Gamma_{\text{crit}}$, compound flows with $\Gamma_n < \Gamma$ are expected to form, because the jet is variable. The neutron component does not participate in internal shocks that develop in variable jets. As a result, neutrons from the slow portions of the jet migrate across the shocks and penetrate the faster portions (Mészáros & Rees 2000). This internal mixing is caused by the short-timescale variability of the central engine that creates a non-uniform flow. The mixing occurs on scales $\delta r \sim r/\Gamma^2$, much smaller than the total thickness of the ejected flow. Large variations of Lorentz factors³ produce a non-uniform compound flow with $\Gamma/\Gamma_n \gg 1$.

Neutron migration can be illustrated by the following simple model. Suppose neutron-loaded flow \mathcal{A} with Lorentz factor $\Gamma_{\mathcal{A}}$ is followed by faster flow \mathcal{B} with Lorentz factor $\Gamma_{\mathcal{B}} \gg \Gamma_{\mathcal{A}}$ (Fig. 2). A shocked region \mathcal{C} forms between the two flows; the shocked plasma has Lorentz factor $\Gamma_{\mathcal{C}}$ such that $\Gamma_{\mathcal{A}} < \Gamma_{\mathcal{C}} < \Gamma_{\mathcal{B}}$. Initially, the neutron component of flow \mathcal{A} is coupled to protons by frequent collisions, so they behave as a single fluid. When neutrons in flow \mathcal{A}

³ Large variations on small scales are suggested by observed variability in GRBs. Large variations also generally help explain the high efficiency of dissipation of internal motions in the jet (e.g. Beloborodov 2000).

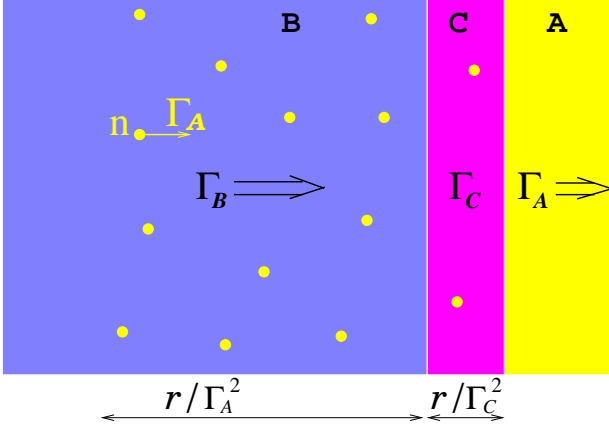


Figure 2. Faster flow \mathcal{B} sweeps slower flow \mathcal{A} and compresses it into a shocked shell \mathcal{C} . Neutrons from flow \mathcal{A} are not swept and instead penetrate flow \mathcal{B} . As a result a compound flow is formed: flow \mathcal{B} contains a slower neutron component with $\Gamma_n = \Gamma_A$. The penetration depth of neutrons is $\sim r/\Gamma_A^2$ in the lab frame; it is $(\Gamma_C/\Gamma_A)^2$ larger than the thickness of shocked region \mathcal{C} .

become collisionally decoupled, they are not swept into region \mathcal{C} anymore. Instead, they penetrate region \mathcal{B} with the relative Lorentz factor $\Gamma_{\text{rel}} = \frac{1}{2}(\Gamma_B/\Gamma_A + \Gamma_A/\Gamma_B) \approx \Gamma_B/2\Gamma_A$. The penetration/mixing length is $\sim (\Gamma_C/\Gamma_A)^2$ larger than the thickness of the shocked region \mathcal{C} .

Some of the penetrating neutrons collide with their new host flow. Each collision dissipates the relative kinetic energy $(\Gamma_{\text{rel}} - 1)m_p c^2$. The number of collisions per baryon of flow \mathcal{B} during the jet expansion timescale equals the collisional ‘optical depth’ of the slow neutrons $\tau_n = n_n \sigma r / \Gamma_n$, where σ is the nuclear cross section. At the beginning of neutron penetration $\tau_n \sim 1$ and a large heat is generated by collisions. The collisions decelerate flow \mathcal{B} from Γ_B to a new Γ , which is found from energy conservation in the static lab frame, $\tau_n \Gamma^2 / 2\Gamma_A \approx \Gamma_B$.⁴ This gives Γ that is lower than the original Γ_B by the factor $(\tau_n \Gamma_B / 2\Gamma_A)^{-1/2}$ as long as $\tau_n > \Gamma_{\text{rel}}^{-1}$.

In summary, GRB jets are expected to contain a significant neutron component (unless they are essentially baryon-free and completely dominated by Poynting flux). At the radius R_n where $\tau_n \sim 1$, collisions between neutrons and protons become rare and compound flows with $\Gamma > \Gamma_n$ inevitably develop. The schematic picture in Figure 3 indicates the main characteristic radii of the jet. The rare nuclear collisions in the region $\tau_n < 1$ dissipate huge energy, comparable to the total energy of the jet. The dissipation efficiency of collisions is $(\Gamma_{\text{rel}} - 1)\tau_n$. It may exceed 100 per cent as the collisionally decelerated jet tends to regain its initial Lorentz factor via adiabatic cooling and re-dissipate its energy. Below we explore how collisional dissipation affects the jet radiation.

4 RADIATIVE MECHANISM

Hereafter we consider a simplified jet model: a neutron component with a single bulk Lorentz factor Γ_n is embedded in a fast proton

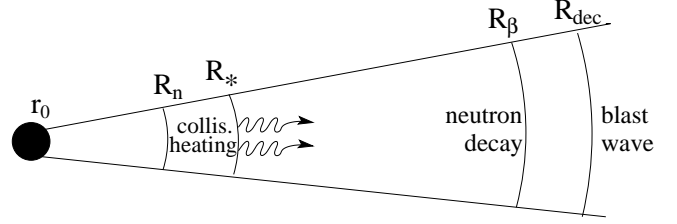


Figure 3. Schematic picture of a baryonic jet. The jet starts to accelerate at radius r_0 . Compound flow with $\Gamma_n < \Gamma$ forms at radius R_n (eq. 6) and strong collisional heating begins at this radius. The jet becomes transparent to radiation at the photosphere $R_* \sim 20R_n$ (eq. 26); its position is regulated by e^\pm creation in the heated region. The figure also shows the mean radius of neutron decay, $R_\beta = 3 \times 10^{15} (\Gamma_n/100)$ cm, and radius R_{dec} where the jet starts to decelerate because of the interaction with an external medium. The photospheric emission is released at R_* , and its spectrum is strongly modified by sub-photospheric collisional heating. Collisional heating continues at $r > R_*$, although with a smaller rate.

component with constant Lorentz factor $\Gamma \gg \Gamma_n$. The proper densities of the neutron and proton components will be denoted by n_n and n , respectively.

4.1 Inelastic nuclear collisions

We consider collisions at radii where $\tau_n = n_n \sigma r / \Gamma_n < 1$,

$$r > R_n \equiv \frac{L_n \sigma}{4\pi m_p c^3 \Gamma_n^3} \approx 5 \times 10^{11} \left(\frac{L_n}{10^{52} \text{ erg/s}} \right) \left(\frac{\Gamma_n}{100} \right)^{-3} \text{ cm}, \quad (6)$$

where $L_n = 4\pi r^2 \Gamma_n^2 n_n m_p c^2$ is the isotropic equivalent of the kinetic luminosity of the neutron flow, and $\sigma \sim 3 \times 10^{-26} \text{ cm}^2$ is the effective cross section for nuclear collisions. The rate of collisions per unit volume (a Lorentz-invariant quantity) is given by

$$\dot{n} = n n_n \Gamma_{\text{rel}} \sigma c. \quad (7)$$

Here $\Gamma_{\text{rel}} = \frac{1}{2}(\Gamma/\Gamma_n + \Gamma_n/\Gamma) \approx \Gamma/2\Gamma_n$ is the relative Lorentz factor of the neutron and proton components of the jet.

Collisions between neutrons and protons occur with significant Γ_{rel} and hence have a large inelastic fraction $f_{\text{inel}} \gtrsim 1/2$ (Amsler et al. 2008). The energy $f_{\text{inel}} \Gamma_{\text{rel}} m_p c^2$ converts to mildly relativistic pions. The data on π^\pm multiplicity in p - p collisions are found in e.g. Breakstone et al. (1984) and refs. therein; a similar multiplicity is expected for n - p collisions. The total π^\pm and π^0 multiplicity is larger by the factor of 3/2; it is typically 5-6 for GRB jets.

The pions immediately decay: $\pi^\pm \rightarrow \mu^\pm + \nu_\mu \rightarrow e^\pm + \nu_e$ and $\pi^0 \rightarrow \gamma + \gamma$. The produced neutrinos escape with observed energies $\sim 0.1\Gamma \text{ GeV}$ and carry away a fraction $f_\nu \sim 1/2$ of the pion energy.⁵ This multi-GeV neutrino emission is an important prediction of the baryonic jet model (Derishev et al. 1999a; Bahcall & Mészáros 2000; Mészáros & Rees 2000), which may be verified

⁴ The decelerated flow with $\Gamma < \Gamma_B$ stores the heat of $\sim (\Gamma/2\Gamma_A)m_p c^2$ per baryon, and later tends to regain its initial Lorentz factor Γ_B as the heat converts back to bulk kinetic energy via adiabatic cooling on the expansion timescale.

⁵ On average, neutrinos take $\sim 3/4$ of π^\pm energy. The average fraction of π^\pm and π^0 energy that is given to neutrinos may be estimated as $f_\nu \sim (2/3)(3/4) = 1/2$.

or dismissed by future neutrino detectors. The existing upper limits from Super-Kamiokande experiment are ~ 10 times above the expected neutrino flux (Fukuda et al. 2002).

The fraction $1 - f_\nu$ of pion energy is given to relativistic e^\pm and high-energy γ -rays, which quickly convert to e^\pm via γ - γ reaction. Thus, the net result of one inelastic collision is the injection of several e^\pm with a Lorentz factor $\gamma_0 \sim m_\pi/m_e \approx 300$ in the rest frame of the plasma flow. The injected e^\pm carry a significant fraction $f_\pm = f_{\text{inel}}(1 - f_\nu) \approx 1/4$ of the collision energy $\Gamma_{\text{rel}} m_p c^2$.

Since neutrons move with a negative radial momentum in the frame of the proton flow, e^\pm are injected with a negative momentum. However, they become quasi-isotropic in the plasma frame after one Larmor rotation in the magnetic field of the jet (the field is transverse to the jet direction; its radial component is strongly suppressed as follows from magnetic flux conservation in the expanding flow). Any reasonable magnetic field advected from the central engine implies a very short gyration timescale $\gamma_0 m_e c / eB$, and the net momentum of injected e^\pm is immediately communicated to the plasma and vanishes in the plasma frame.

The energy of e^\pm injected per unit volume per unit time equals $f_\pm \Gamma_{\text{rel}} m_p c^2 \dot{n}$. Practically all of this energy is quickly converted to radiation (see Section 4.2). As a result, radiation accumulates energy density with rate (measured in the plasma rest frame),

$$\dot{Q}_{\text{nth}} = f_\pm \Gamma_{\text{rel}} m_p c^2 \dot{n}. \quad (8)$$

Here subscript ‘nth’ stands for radiation produced by nonthermal e^\pm that are generated by nuclear collisions. Using equation (7) and $\dot{Q}_{\text{nth}} = c\Gamma dQ_{\text{nth}}/dr$, one finds

$$\frac{1}{nm_p c^2} \frac{dQ_{\text{nth}}}{d \ln r} = \frac{f_\pm}{4} \frac{\Gamma}{\Gamma_n} \tau_n \approx \frac{1}{16} \frac{\Gamma}{\Gamma_n} \frac{R_n}{r}. \quad (9)$$

4.2 Radiative cooling of injected e^\pm

The e^\pm pairs injected by nuclear collisions have a large Lorentz factor $\gamma_0 \sim m_\pi/m_e$ and immediately radiate their energy via Compton and/or synchrotron cooling.

4.2.1 Compton cooling

The timescale for Compton cooling of an electron with Lorentz factor γ by radiation with energy density U_γ is⁶

$$t_C = \frac{3m_e c}{4U_\gamma \sigma_T \gamma}. \quad (10)$$

Radiation is initially present in GRB jets (Section 2), and U_γ is further increased as the radiation absorbs the energy of injected e^\pm . Compton cooling timescale is shorter than the timescale of jet expansion $t_{\text{exp}} = r/c\Gamma$. Their ratio is

$$\frac{t_C}{t_{\text{exp}}} = \frac{3}{4l\gamma}, \quad (11)$$

where

$$l \equiv \frac{U_\gamma}{m_e c^2} \sigma_T \frac{r}{\Gamma} \quad (12)$$

⁶ This estimate assumes Thomson scattering, i.e. neglects the Klein-Nishina correction to the scattering cross section. The peak of GRB radiation is $E'_{\text{peak}} \sim \text{MeV}/\Gamma \sim \text{keV}$ in the jet frame. Since $E'_{\text{peak}} \gamma < m_e c^2$ for all $\gamma \leq \gamma_0$, most of the scattering by e^\pm occurs in Thomson regime. Exact calculations of radiative transfer with the full Klein-Nishina cross section are performed in Section 5.

is the dimensionless ‘compactness’ parameter of the radiation field. One can express l as

$$l = \frac{m_p}{m_e} \epsilon \tau_p, \quad \epsilon \equiv \frac{U_\gamma}{nm_p c^2}. \quad (13)$$

Here ϵ is the fraction of the jet energy that is carried by radiation ($\epsilon > 0.1$ for the model proposed in this paper), and

$$\tau_p \equiv \frac{\sigma_T n r}{\Gamma} = \frac{\sigma_T}{\sigma} \frac{n}{n_n} \frac{\Gamma_n}{\Gamma} \tau_n \approx \left(\frac{L}{5L_n} \right) \left(\frac{\Gamma}{5\Gamma_n} \right)^{-3} \tau_n. \quad (14)$$

The compactness l is high in the main heating region $\tau_n \lesssim 1$, and hence Compton cooling is fast, $t_C \ll t_{\text{exp}}$.

The high compactness has another implication. Photons that are scattered by relativistic e^\pm to energies $E' \gg 1$ MeV in the jet frame will not survive – they will convert to secondary e^\pm via reaction $\gamma + \gamma \rightarrow e^+ + e^-$. The development of e^\pm cascade that accompanies Compton cooling of relativistic particles (Appendix A) is described in detail by Svensson (1987) and Lightman & Zdziarski (1987). In this paper, the cascade is modeled numerically with our Monte-Carlo code. The typical multiplicity of secondary e^\pm \mathcal{M}_s is comparable to 60. The total multiplicity of e^\pm created following one nuclear collision is

$$\mathcal{M} = \mathcal{M}_0 \mathcal{M}_s \sim 10^2, \quad (15)$$

where

$$\mathcal{M}_0 = \frac{f_\pm \Gamma_{\text{rel}} m_p}{\gamma_0 m_e} \sim \frac{3}{4} \frac{\Gamma}{\Gamma_n} \quad (16)$$

is the multiplicity of ‘primary’ e^\pm injected with Lorentz factor $\gamma_0 \sim m_\pi/m_e$ following a nuclear collision.

4.2.2 Synchrotron cooling

In the presence of magnetic fields, the injected e^\pm also experience synchrotron losses. The synchrotron cooling timescale is similar to equation (10) except that U_γ in this equation is replaced by the magnetic energy density $U_B = B^2/8\pi$ (measured in the jet frame). The synchrotron losses dominate if $U_B > U_\gamma$. U_B may be expressed as

$$U_B = \frac{B^2}{8\pi} = \frac{\epsilon_B L}{4\pi r^2 \Gamma^2 c}, \quad (17)$$

where ϵ_B is the magnetic fraction of the jet energy. The typical energy of synchrotron photons in the plasma frame is $E'_s = 0.3 \gamma_0^2 \hbar e B / m_e c$. The corresponding energy in the lab frame, $E_s \approx \Gamma E'_s$, is given by

$$E_s \approx 0.3 \gamma_0^2 \frac{\hbar e}{m_e c r} \left(\frac{2\epsilon_B L}{c} \right)^{1/2} \approx 200 r_{12}^{-1} \epsilon_B^{1/2} L_{52}^{1/2} \text{ keV}, \quad (18)$$

where we substituted $\gamma_0 \approx m_\pi/m_e \approx 300$. Synchrotron emission peaks in the region $r \gtrsim R_n$ where heating peaks and most of e^\pm are injected. Jets for which synchrotron cooling is significant (i.e. where it can compete with Compton cooling) have large ϵ_B ; then E_s is comparable to the typical E_{peak} of observed GRB spectra. A similar $E_s \sim E_{\text{peak}}$ was found by Koers & Giannios (2007). This feature of collisionally heated jets offers an additional mechanism for the preferential peak position at 0.1–1 MeV.

Synchrotron emission from particles with low $\gamma \lesssim 5$ is self-absorbed. These particles cannot be cooled by the synchrotron mechanism; they are Compton cooled.

4.3 Optical depth of the jet

In view of the strong e^\pm loading and the large cross section for photon scattering $\sigma_T \gg \sigma$, one may expect a large optical depth τ_T where the bulk of nuclear collisions occur. Note, however, that $\tau_T \propto \Gamma^{-3}$ while $\tau_n \propto \Gamma_n^{-3}$. In compound flows $(\Gamma/\Gamma_n)^{-3} \ll 1$; as a result, the collisionally heated jet with $\tau_n \lesssim 1$ has a moderate τ_T .

If no e^\pm pairs were created, the optical depth of the compound flow would equal τ_p (eq. 14), which may be smaller than unity at $r \gtrsim R_n$. The actual optical depth is enhanced and dominated by e^\pm created by the nonthermal cascade (Derishev et al. 1999a). The continually injected e^\pm quickly cool down and accumulate at relatively low energies, forming a thermalized population that maintains a Maxwellian distribution via frequent Coulomb collisions between e^\pm . It is convenient to express the rate of e^\pm supply as

$$\dot{n}_\pm = \mathcal{M} \dot{n} = \frac{Y \dot{Q}_{\text{nth}}}{m_e c^2}, \quad (19)$$

where $\dot{Q}_{\text{nth}} = f_\pm \Gamma_{\text{rel}} m_p c^2 \dot{n}$ is the rate of energy injection in primary e^\pm , and $Y = \mathcal{M}_s/\gamma_0$ is the ‘pair yield’ of the cascade. A minimum $Y_{\text{min}} \sim \gamma_0^{-1}$ would be obtained when counting only the primary e^\pm from pion decay. This may be appropriate for very strongly magnetized jets where synchrotron cooling of e^\pm strongly dominates over Compton cooling ($U_B \gg U_\gamma$) and suppresses the e^\pm cascade. In weakly magnetized jets with $U_B < U_\gamma$, the development of e^\pm cascade gives $Y = \mathcal{M}_s/\gamma_0 \sim 0.2$.

Let n_\pm be the density of accumulated thermalized pairs. Their annihilation rate is given by

$$\dot{n}_{\text{ann}} = \frac{3}{16} \sigma_T c n_\pm^2. \quad (20)$$

This expression assumes $n_\pm > n$ and $kT < m_e c^2$; both assumptions are valid where annihilation is significant. The density of accumulated e^\pm evolves according to equation

$$\frac{\Gamma c}{r^2} \frac{d}{dr} (r^2 n_\pm) = \dot{n}_\pm - \dot{n}_{\text{ann}}. \quad (21)$$

At the beginning of collisional heating, \dot{n}_\pm and \dot{n}_{ann} are both larger than the left side of equation (21), and the equilibrium $\dot{n}_\pm \approx \dot{n}_{\text{ann}}$ is established,

$$Y f_\pm \Gamma_{\text{rel}}^2 \frac{m_p}{m_e} \sigma c n n = \frac{3}{16} \sigma_T c n_\pm^2, \quad (22)$$

which gives

$$\tau_T(r) \equiv \frac{n_\pm \sigma_T r}{\Gamma} = \left(\frac{4}{3} \frac{m_p}{m_e} \frac{\sigma_T}{\sigma} f_\pm Y \frac{L}{L_n} \right)^{1/2} \frac{\Gamma_n}{\Gamma} \tau_n, \quad (23)$$

or, using $\tau_n = R_n/r$ and $f_\pm \approx 1/4$,

$$\tau_T(r) = \tau_0 \frac{R_n}{r}, \quad \tau_0 \approx 20 \left(\frac{Y}{0.2} \right)^{1/2} \left(\frac{L}{5L_n} \right)^{1/2} \left(\frac{\Gamma}{5\Gamma_n} \right)^{-1}. \quad (24)$$

τ_T stays near the equilibrium value $\propto \tau_n$ even after the annihilation timescale becomes long and the e^\pm population freezes-out. This is the result of a coincidence: the annihilation equilibrium gives $\tau_T \propto r^{-1}$, which is also maintained when $\dot{n}_\pm = \dot{n}_{\text{ann}} = 0$. Therefore, equation (24) remains valid even at late stages when the jet becomes transparent to radiation.

The e^\pm optical depth is maximum at the beginning (and peak) of collisional dissipation when $\tau_n \sim 1$. At this stage, Γ/Γ_n is limited by the deceleration effect of collisions (see the end of Section 3). In particular, the collision of flows \mathcal{A} and \mathcal{B} considered in Section 3 gives a compound flow with $L \sim L_B$, $L_n \sim L_A$, and $\Gamma/\Gamma_n \sim (\Gamma_B/\Gamma_A)^{1/2}$ at $r \gtrsim R_n$. Then equation (24) gives

$$\tau_0 \sim 20 \left(\frac{Y}{0.2} \right)^{1/2} \left(\frac{\Gamma_A}{\Gamma_B} \frac{L_B}{L_A} \right)^{1/2}. \quad (25)$$

It is reasonable to suppose $L_B/L_A > 1$ when $\Gamma_B/\Gamma_A > 1$ and expect $(\Gamma_B L_A/\Gamma_B L_B)^{1/2} \sim 1$ within a factor of a few.

The result may be summarized by the simple approximate formula $\tau_T(x) \sim 20(Y/0.2)^{1/2} x^{-1}$, where $x = r/R_n$. This estimate is a rather crude approximation (e.g. it neglects the moderate adiabatic acceleration of the collisionally heated jet), yet it demonstrates an important feature: $\tau_T(x)$ weakly depends on the parameters of the jet, as long as $\Gamma \gg \Gamma_n$. The estimate of τ_T also gives a simple expression for the photospheric radius,

$$R_\star = \tau_0 R_n \sim 20 \left(\frac{Y}{0.2} \right)^{1/2} R_n. \quad (26)$$

The radiation produced by collisional heating in the opaque region $R_n < r < R_\star$ is not buried by the optical depth. As demonstrated by the radiative transfer simulations in Section 5, it creates a powerful burst escaping to distant observers.

4.4 Coulomb heating of thermalized e^\pm by ions

The thermalized e^\pm population naturally tends to acquire the so-called Compton temperature in the radiation field, T_C , at which Compton cooling is balanced by Compton heating due to quantum recoil in scattering (e.g. Rybicki & Lightman 1979). If no mechanism heats e^\pm , they would quickly reach Compton equilibrium with $kT_e = kT_C \sim 1$ keV. This however does not happen, because thermal e^\pm are continually heated by Coulomb collisions with protons. As a result, the e^\pm temperature T_e is maintained above T_C . Its value is calculated below; it satisfies $kT_C \ll kT_e \ll m_e c^2$ in the sub-photospheric heating region.

Nuclear collisions with $\Gamma_{\text{rel}} > 1$ inevitably heat the proton component of the jet to a relativistic temperature.⁷ The stirred protons acquire a non-Maxwellian distribution with a large fraction of protons having kinetic energies $\gtrsim m_p c^2$. The temperature of the accumulated e^\pm population is kept at a much smaller value by Compton cooling. In this ‘two-temperature’ plasma, Coulomb collisions tend to transfer energy from protons to e^\pm . The thermal velocity of e^\pm is well below c and they may be approximated as cold ($T_e = 0$) when calculating the Coulomb energy losses of the energetic protons. A proton with velocity β_p in the jet rest frame passes its energy to the cold e^\pm background with rate (e.g. Ginzburg & Syrovatskii 1964)

$$\dot{E}_{\text{Coul}} = \frac{3}{2} \ln \Lambda \frac{\sigma_T n_\pm m_e c^3}{\beta_p}, \quad (27)$$

where $\beta_p \sim 1$, $\ln \Lambda = \ln(m_e c^2/\hbar \omega_p) \approx 20$ is the Coulomb logarithm, and $\omega_p = (4\pi n_\pm e^2/m_e)^{1/2}$. The net rate of energy transfer from protons to the thermal e^\pm plasma is

$$\dot{Q}_{\text{th}} \approx \frac{3}{2} \ln \Lambda n \sigma_T n_\pm m_e c^3, \quad (28)$$

which gives

$$\frac{1}{n m_p c^2} \frac{dQ_{\text{th}}}{d \ln r} \approx \frac{3}{2} \ln \Lambda \frac{m_e}{m_p} \tau_T \approx 0.02 \tau_T. \quad (29)$$

It is useful to compare \dot{Q}_{th} with \dot{Q}_{nth} (Section 4.1). From equations (9), (29), and (24) one finds,

⁷ Nuclear collisions also create a hot neutron component moving with the bulk Lorentz factor Γ .

$$\frac{\dot{Q}_{\text{th}}}{\dot{Q}_{\text{nth}}} \approx \left(\frac{L}{5L_n}\right)^{1/2} \left(\frac{\Gamma}{5\Gamma_n}\right)^{-2} \left(\frac{Y}{0.1}\right)^{1/2}. \quad (30)$$

The thermal and nonthermal heating rates are comparable.

The e^\pm do not keep the heat Q_{th} received from protons. Instead, they immediately pass it to radiation via Compton scattering and remain at a temperature $kT_e \ll Q_{\text{th}}/n_\pm$. The value of T_e is found from the balance between Coulomb heating and Compton cooling of e^\pm ,

$$\frac{3}{2} n_\pm \frac{k(T_e - T_C)}{t_C} = \dot{Q}_{\text{th}}, \quad (31)$$

where t_C is given by equation (10) with $\gamma \approx 1$. We have neglected the adiabatic cooling of e^\pm because its rate is smaller than Coulomb heating and Compton cooling rates by the factor $t_C/t_{\text{exp}} \ll 1$. Then we find

$$\Theta_e \equiv \frac{kT_e}{m_e c^2} \approx \frac{3m_e}{4m_p} \frac{\ln \Lambda}{\epsilon} + \frac{kT_C}{m_e c^2} \approx \frac{0.01}{\epsilon} + \Theta_C, \quad (32)$$

where $\Theta = kT_C/m_e c^2$ is the dimensionless Compton temperature of the radiation field; $\Theta_C \approx 0.007$ for the radiation spectrum calculated below (Fig. 5).

Kompaneets' y -parameter of thermal e^\pm is given by

$$y = 4\tau_T(\Theta_e - \Theta_C) \approx \frac{0.04\tau_0}{\epsilon} \frac{R_n}{r}. \quad (33)$$

It is comparable to or below unity which shows that Compton cooling of e^\pm occurs in the unsaturated regime. Thermal Comptonization has an important effect on the radiation spectrum, which is computed in Section 5.

4.5 Distribution function of e^\pm

The local distribution function of e^\pm is shaped by the processes of e^\pm injection, cooling and thermalization, and Coulomb heating of thermalized e^\pm by protons. The distribution is quasi-steady, i.e. it is established at a given radius on a timescale much shorter than the expansion timescale of the jet. It gradually changes as the jet expands. Figure 4 shows the momentum distribution of e^\pm at radius $r = 4R_n$ for a typical jet model. The jet has the same parameters as in Figure 1 except that it now carries neutrons with $\Gamma_n = 100$ and $L_n = 2 \times 10^{51}$ erg/s. Synchrotron cooling was neglected in this example, i.e. the jet was assumed to be weakly magnetized, $\epsilon_B \ll 1$. The distribution has been calculated by the Monte-Carlo code described in Appendix B. The temperature of the thermal part $\Theta_e \approx 0.03$ is consistent with the analytical result (eq. 32); it is self-regulated so that the balance is maintained between Coulomb heating and Compton cooling. The nonthermal part of the distribution is formed by the e^\pm cascade that results from e^\pm injection with $\gamma_0 \approx m_\pi/m_e$.

For comparison, the dotted curve in Figure 4 shows the electron distribution that is found at the same radius in the passively cooling neutron-free jet. The distribution is Maxwellian, and its temperature equals the temperature of the (Planckian) radiation field.

4.6 Radiative efficiency of photospheric emission

The evolution of radiation density U_γ (measured in the plasma co-moving frame) is given by equation

$$\frac{1}{r^2} \frac{d}{d \ln r} (r^2 U_\gamma) = \left(\frac{dU_\gamma}{d \ln r} \right)_{\text{ad}} + \frac{dQ_{\text{th}}}{d \ln r} + \frac{dQ_{\text{nth}}}{d \ln r}. \quad (34)$$

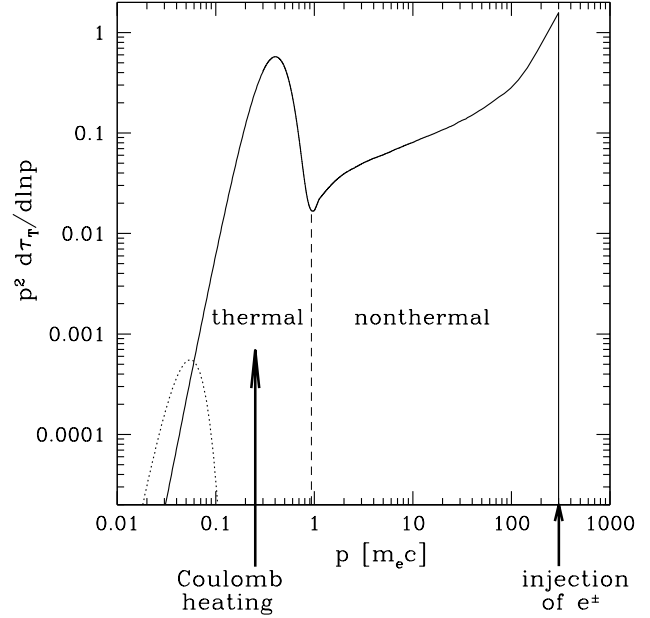


Figure 4. Momentum distribution of e^\pm . Dotted curve shows the case of a passively cooling jet (the model with $\Gamma = 600$ from Fig. 1). Solid curve shows the case of a collisionally heated jet at the same radius (see text). The distribution was calculated at $r = 4R_n$. Vertical dashed line indicates the boundary between the thermal and nonthermal parts of the distribution. The two parts make comparable contributions to the Compton amplification factor $A \sim \int p^2 (d\tau_T/dp) dp \sim 1$ that measures the average energy boost of photons in one scattering by the e^\pm plasma. The total/integrated optical depth τ_T at this radius is $\tau_T = 5$; it is strongly dominated by the thermal part of the distribution.

The first term on the right side of this equation describes the adiabatic cooling of radiation; it equals $-(2/3)U_\gamma$ in the opaque zone and 0 in the transparent zone (the exact behavior of this term near photosphere is obtained from the numerical simulation of radiative transfer). The second and third terms on the right side represent the energy received by e^\pm plasma and converted to radiation. Since practically all of the energy received by e^\pm is passed to radiation, these terms effectively serve as sources of radiation energy. Heating of the thermalized e^\pm population by Coulomb collisions with protons $dQ_{\text{th}}/d \ln r$ is given by equation (29). Energy injection into the nonthermal e^\pm tail $dQ_{\text{nth}}/d \ln r$ is given by equation (9). Substituting these expressions to equation (34) we obtain the equation for $\epsilon \equiv U_\gamma/nm_p c^2$,

$$x \frac{d\epsilon}{dx} = -q(x)\epsilon + \frac{a_{\text{th}} + a_{\text{nth}}}{x}, \quad (35)$$

where $a_{\text{th}} = 0.02\tau_0$ and $a_{\text{nth}} = f_\pm \Gamma_{\text{rel}}/2$ are constants, $x \equiv r/R_n$, and $q(x) \equiv -(d \ln U_\gamma / d \ln r)_{\text{ad}}$ is a dimensionless function that equals $2/3$ in the optically thick zone $\tau_T \gg 1$ and approaches 0 at the photosphere. The quantity ϵ is the fraction of the jet energy carried by radiation; it can also be written in the lab frame as

$$\epsilon = \frac{L_\gamma}{L}, \quad (36)$$

where $L_\gamma = 4\pi r^2 \Gamma^2 U_\gamma c$ is the isotropic equivalent of radiation luminosity, and $L = 4\pi r^2 \Gamma^2 n m_p c^3$ is the isotropic equivalent of the jet kinetic luminosity.

In the optically thick zone, where $q \approx 2/3$, equation (35) can be solved analytically for $\epsilon(x)$,

$$\epsilon(x) = \frac{\epsilon_1 + 3a}{x^{2/3}} - \frac{3a}{x}, \quad 1 < x < \frac{R_\star}{R_n}, \quad (37)$$

where $\epsilon_1 \equiv \epsilon|_{r=R_n}$ and $a = a_{\text{th}} + a_{\text{nth}}$. The solution may be used to estimate ϵ at the photosphere, $x_\star = R_\star/R_n = \tau_0$. For jets with small ϵ_1 one obtains

$$\epsilon_\star \approx \left(0.06 \tau_0^{1/3} + \frac{0.2}{\tau_0^{2/3}} \frac{\Gamma}{\Gamma_n} \right) \left(1 - \frac{1}{\tau_0^{1/3}} \right), \quad (38)$$

where $\tau_0 \sim 20(Y/0.2)^{1/2}$ (Sect. 4.3). Equation (38) estimates the net radiative efficiency of collisional heating in jets with $\Gamma \gg \Gamma_n$, taking into account the adiabatic cooling of radiation until the jet expands to transparency.⁸ For example, $\tau_0 = 20$ gives $\epsilon_\star \approx 0.1 + 0.02\Gamma/\Gamma_n$. The two terms represent the contributions from the Coulomb heating of thermalized e^\pm and the nonthermal e^\pm injection. For typical $\Gamma/\Gamma_n \sim 3 - 10$ the total radiative efficiency $\epsilon_\star = 0.2 - 0.3$, with the thermal part comparable to the nonthermal part (cf. also eq. 30).

5 RADIATION SPECTRA FROM COLLISIONALLY HEATED JETS

5.1 Thermal and nonthermal Comptonization

Suppose the jet cools passively at $r < R_n$ and its thermal radiation evolves as described in Section 2. The collisional heating begins at radius R_n (eq. 6) and quickly loads the jet with energetic e^\pm ; their typical distribution function is shown in Figure 4. Scattering of radiation by the injected e^\pm dramatically changes the photon spectrum.

Consider a weakly magnetized jet with $U_B \ll U_\gamma$, when the synchrotron cooling of e^\pm is negligible. Then the GRB spectrum forms via Comptonization of already existing thermal photons advected from the center of the explosion. Scattering conserves photon number and the average photon energy \bar{E} in the lab frame can be expressed as (cf. eqs. 2 and 3)

$$\bar{E} = \frac{\epsilon \Gamma n m_p c^2}{n_\gamma} = \epsilon \bar{E}_0 \approx 4 \epsilon r_{0,7}^{-1/2} L_{52}^{1/4} \text{ MeV}, \quad (39)$$

where $\epsilon = L_\gamma/L$ is the fraction of jet energy carried by radiation. The relation (39) is common for all Comptonization models of GRBs (e.g. Thompson 1994; Rees & Mészáros 2005; Giannios & Spruit 2007). It naturally explains the observed $\bar{E} \sim \text{MeV}$, assuming a reasonable radiative efficiency $\epsilon \gtrsim 0.1$. In the collisionally heated jet, \bar{E} grows as photons receive energy via two branches of heating: thermal and nonthermal (Section 4). The corresponding heating rates *per photon* give

$$\left(\frac{d\bar{E}}{d \ln r} \right)_{\text{th}} \approx 0.02 \tau_0 \bar{E}_0 \frac{R_n}{r}, \quad (40)$$

$$\left(\frac{d\bar{E}}{d \ln r} \right)_{\text{nth}} \approx \frac{1}{16} \frac{\Gamma}{\Gamma_n} \bar{E}_0 \frac{R_n}{r}, \quad (41)$$

⁸ Equation (38) assumes the adiabatic cooling $\propto r^{-2/3}$ at all $r < R_\star$. It overestimates the cooling effect – the exact radiative transfer gives less cooling (see Section 2). Therefore, equation (38) underestimates ϵ_\star by a factor ~ 2 .

where \bar{E}_0 is given by equation (3). The heating rates and the adiabatic cooling determine the evolution of $\bar{E}(r)$ in the collisionally heated jet.⁹ However, the known \bar{E} does not yet determine the shape of the radiation spectrum. The spectrum depends on the details of Comptonization that need to be calculated.

The radiation spectra produced by Compton cooled e^\pm cascades were previously studied in detail in the context of AGN accretion discs (e.g. Svensson 1987; Lightman & Zdziarski 1987; see also Appendix A). The model was developed for static sources, and Comptonization of radiation in relativistic flows is different for two reasons. First, the optical depth evolves as the flow expands. Second, the GRB radiation moves together with the plasma and remains embedded in it until the jet reaches $r \sim R_\Delta \sim \Gamma^2 \Delta \sim 10^{16} \text{ cm}$ (here $\Delta/c \sim 1 - 10 \text{ s}$ is the typical duration of GRB jets). Collisional heating operates at smaller radii $r < R_\Delta$, and the entire history of heating and Comptonization is ‘recorded’ in the radiation field before it escapes the jet. The spectrum received by distant observers is the net result of multi-radius (multi-optical-depth) Comptonization in the expanding jet. In this respect, GRBs are similar to the relict radiation in the expanding universe.

The cooling rate of e^\pm and their energy distribution at any given location depend on the local radiation field. Therefore, the evolution of radiation and e^\pm plasma must be calculated together. This is performed by the numerical code described in Appendix B. The code is based on the Monte-Carlo method that solves the radiative transfer in a jet with self-consistent e^\pm distribution function. For a given history of heating, the code calculates the evolution of e^\pm and radiation in the expanding flow and finds the spectrum of photons escaping to distant observers.

As a typical example, consider the jet model from Section 2 with $\Gamma = 600$, $L = 10^{52} \text{ erg/s}$, and $r_0 = 10^7 \text{ cm}$, but now let it contain a neutron component with $\Gamma_n = 100$ and $L_n = 2 \times 10^{51} \text{ erg/s}$. The collisional heating in this fiducial model begins at radius $R_n \approx 10^{11} \text{ cm}$ (eq. 6). Just before the onset of heating and e^\pm creation, the passively cooling jet has $\bar{E}(R_n) \approx 1 \text{ MeV}$. The optical depth after the onset of collisional heating is $\tau_{\text{T}}(r) = (R_n/r)\tau_0$ with $\tau_0 \approx 20$ (eq. 24). The heating rates in equations (40) and (41) happen to be almost exactly equal: $(d\bar{E}/d \ln r)_{\text{nth}} \approx (d\bar{E}/d \ln r)_{\text{th}} \approx 1.5 (R_n/r) \text{ MeV}$.

Figure 5 shows the spectrum of emitted radiation for the fiducial model. Although it may not be obvious from the figure, the Comptonized spectrum has two components, which correspond to the two parts of the e^\pm distribution function (cf. Fig. 4):

(i) Most photons are multiply scattered by the thermalized Coulomb-heated e^\pm population and never scattered by the optically thin nonthermal tail. This thermal Comptonization dominates the emitted spectrum at energies up to $2\Gamma kT_e \sim 20 \text{ MeV}$ and creates the spectrum slope $\beta \sim -(2.5 - 3)$. It corresponds to Kompaneets’ parameter $y \sim 1$ that is regulated in the heated jet as discussed in Section 4.4.

(ii) A small fraction of photons are additionally scattered by the nonthermal tail of e^\pm distribution, which strongly boosts their energy. The nonthermal component dominates the radiation spectrum at high energies.

A special feature of collisional heating is that the energy of the two spectral components are comparable (eq. 30). The nonthermal component smoothly extends the spectrum through 100 MeV to

⁹ Since $\bar{E}/\bar{E}_0 = \epsilon$ for a jet with a conserved photon number, the equation for $\bar{E}(r)$ is immediately obtained from eq. (35).

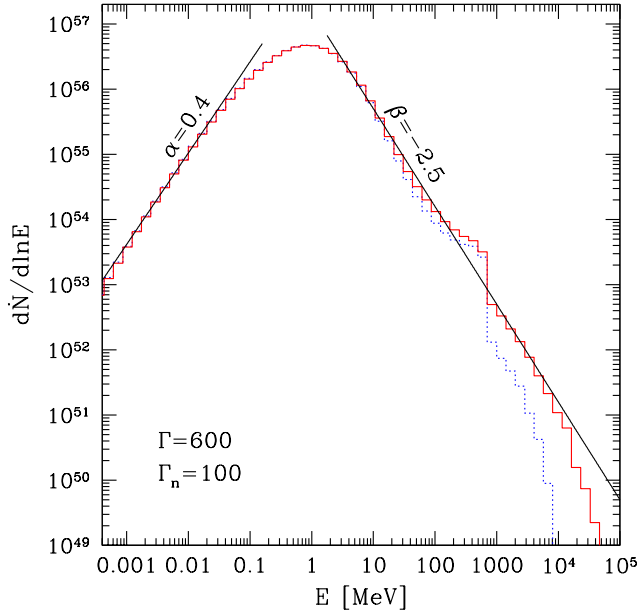


Figure 5. Photon spectrum emitted by the collisionally heated jet (solid red histogram). The jet has $L = 10^{52}$ erg/s, $r_0 = 10^7$ cm, $\Gamma = 600$ (same as in Fig. 1), and carries neutrons with $\Gamma_n = 100$. Black solid lines indicate the slopes that correspond to photon indices $\alpha = 0.4$ and $\beta = -2.5$. A similar phenomenological spectrum is usually proposed to fit GRB observations (Band et al. 2009). The feature near 0.5 GeV is the annihilation line. Dotted blue histogram shows the spectrum that would be produced if nuclear collisions were ‘switched off’ at $r > 4R_n = 0.2R_*$, i.e. if e^\pm injection was confined to radii $R_n < r < 4R_n$. The figure does not take into account the cosmological redshift of the burst z ; the redshifted spectrum will peak at $(1+z)^{-1}$ MeV instead of 1 MeV.

the GeV range. It is broad and additionally smoothed by partial downscattering in the optically thick plasma before the jet expands to transparency.

Most of collisional heating and Comptonization occurs where the jet is still opaque. The Comptonized radiation is released at the photosphere R_* and can be called ‘photospheric emission’ (but see Section 5.3 below). The average energy of escaping photons in the model shown in Figure 5 is $\bar{E} \approx 2$ MeV, which is half of $\bar{E}_0 \approx 4$ MeV. This means that the net radiation efficiency of the burst is $\sim 50\%$, i.e. the photospheric emission carries about half of the jet energy.¹⁰

The ratio of the thermal and nonthermal Comptonization components in the observed spectrum is controlled by the parameter $w \approx 3\tau_0^{-1}\Gamma/\Gamma_n$ (the ratio of eqs. 40 and 41), where τ_0 is likely to stay around 20 within a factor of a few as long as the condition $\Gamma \gg \Gamma_n$ is satisfied (Section 4.3). To investigate the sensitivity of the model predictions to expected variations in w , we calculated three models with equal $\tau_0 = 20$ and different $\Gamma/\Gamma_n = 3, 6$ and 12. They have $w \approx 0.5, 1$ and 2, correspondingly. We found similar spectra in all three cases, with slightly different indices $\beta \sim 2.5 \pm 0.2$. With increasing w , the nonthermal bump becomes

more pronounced. Large $w \gg 1$ are not, however, plausible (strong nonthermal heating is always accompanied by significant Coulomb heating in a realistic jet model). Small w are possible: w can jump to zero if Γ/Γ_n decreases so that nuclear collisions become unable to produce pions. This case is discussed in Section 5.4 below.

5.2 Annihilation line

The annihilation reaction between thermalized e^\pm produces photons with energy $E' \approx m_e c^2$ in the rest frame of the jet. The number flux of annihilation photons (isotropic equivalent) in the lab frame is given by $\dot{N}_{\text{ann}} = 4\pi r^2 c \Gamma n_{\text{ann}}$, where n_{ann} is the density of annihilation photons in the jet frame. It obeys the equation,

$$\frac{d\dot{N}_{\text{ann}}}{dr} = 4\pi r^2 \dot{n}_{\text{ann}}. \quad (42)$$

Using equations (20) and (24) one finds

$$\frac{d\dot{N}_{\text{ann}}}{dx} = \frac{3\pi}{4} \frac{c\tau_0^2}{x^2} \frac{\Gamma^2}{\sigma_T} R_n, \quad (43)$$

where $x = r/R_n > 1$ and τ_0 is given by equations (23), (24). Integrating equation (43) over x , one finds the net flux of annihilation photons emitted to infinity,

$$\dot{N}_{\text{ann}} = \frac{f_\pm Y}{4\Gamma_n} \frac{L}{m_e c^2}. \quad (44)$$

It is instructive to compare this result with the number flux of original thermal photons in the jet, \dot{N} ,

$$\frac{\dot{N}_{\text{ann}}}{\dot{N}} = \frac{f_\pm Y}{4\Gamma_n} \frac{\bar{E}_0}{m_e c^2} \approx 2.5 \times 10^{-4} \left(\frac{\Gamma_n}{100} \right)^{-1} \left(\frac{Y}{0.2} \right) \left(\frac{\bar{E}_0}{\text{MeV}} \right). \quad (45)$$

For our fiducial model shown in Figure 5, $\dot{N}_{\text{ann}}/\dot{N} \approx 10^{-3}$ creates a rather strong annihilation line that cuts off at $E = 2\Gamma m_e c^2$. Most of the annihilation photons are produced well below the photosphere. The resulting spectral feature has an extended red wing due to Compton downscattering in the sub-photospheric region and the variation in the Doppler boost, which depends on the photon angle at the emission (or last-scattering) point.

In strongly magnetized jets, where synchrotron cooling dominates over Compton cooling, the pair yield Y is reduced (Section 4.3) and the annihilation feature will be weak.

5.3 $\gamma\gamma$ opacity and emission at energies $E \gg \text{GeV}$

To a first approximation, one could neglect the heating at radii $r \gg R_n$, and a similar spectrum would be obtained. For instance, suppose that nuclear collisions occur only in the region $R_n < r < 4R_n$. The result is shown by the dotted curve in Figure 5. The spectrum is significantly changed only at high energies: the number of photons above the threshold for pair creation is suppressed. This suppression is caused by the large compactness l at small radii, which implies a large optical depth to $\gamma\gamma$ absorption, $\tau_{\gamma\gamma} \gg 1$.

The extension of the spectrum to ~ 100 GeV in the full model (solid curve) is due to the extension of nuclear collisions to large radii $r \sim 10^3 R_n$, where $\tau_{\gamma\gamma}$ becomes small and high-energy photons are able to escape.¹¹ The smaller rate of nonthermal heating at large r is compensated by the $\gamma\gamma$ transparency at high energies. As

¹⁰ The energy given to photons by collisional heating in the region $R_n < r < R_*$ is 2×1.5 MeV in the model shown in Fig. 5. Together with the initial 1 MeV per photon at R_n this would make $\bar{E} = 4$ MeV, if there were no adiabatic cooling. Adiabatic cooling at $r < R_*$ reduces \bar{E} by a factor of 2.

¹¹ I thank Indrek Vurm for pointing out the effect of continued collisional heating at large r on the spectrum shape in the GeV range.

a result, $\sim 10^{-3}$ of the jet energy is converted to escaping photons with energy comparable to 100 GeV.

A simple analytical estimate for the optical depth seen by a photon of energy E at a radius r is given by,

$$\tau_{\gamma\gamma}(E, r) = \frac{\sigma_{\gamma\gamma} d\dot{N}/d\ln E_t}{4\pi r c \Gamma^2}. \quad (46)$$

Here $\sigma_{\gamma\gamma} \approx 10^{-25} \text{ cm}^2$ is the average cross-section for $\gamma\text{-}\gamma$ absorption by the target photons near the threshold, $E_t/m_e c^2 \sim 2\Gamma^2(E/m_e c^2)^{-1}$. This estimate assumes a typical angle $\theta \sim \Gamma^{-1}$ between the interacting photons. Approximating the spectrum of target photons by the Band function with $E_{\text{peak}} \sim 1 \text{ MeV}$, one finds at $E_t > E_{\text{peak}}$

$$\frac{d\dot{N}}{d\ln E_t} \approx 3 \times 10^{57} \left(\frac{E_t}{m_e c^2} \right)^{1+\beta} L_{\gamma,52} \text{ s}^{-1}, \quad (47)$$

where L_γ is the total photon luminosity (isotropic equivalent). This gives,

$$\tau_{\gamma\gamma}(E, r) \approx \frac{2 \times 10^3}{40^{-\beta-1}} r_{12}^{-1} L_{\gamma,52} \left(\frac{E}{10 \text{ GeV}} \right)^{-\beta-1} \left(\frac{\Gamma}{600} \right)^{2\beta}. \quad (48)$$

For the typical $\beta \approx -2.5$, the radius of $\gamma\text{-}\gamma$ transparency (where $\tau_{\gamma\gamma} = 1$) is given by

$$R_{\gamma\gamma}(E) \sim 10^{13} \left(\frac{E}{10 \text{ GeV}} \right)^{1.5} \left(\frac{\Gamma}{600} \right)^{-5} L_{\gamma,52} \text{ cm}. \quad (49)$$

The target photons absorbing 10-100-GeV photons have sub-GeV energy. Most of them are emitted at $r \sim R_*$ and hence the target radiation field at $r \gg R_*$ is strongly collimated along the radial direction in the jet frame. This creates an “escape cone” for the high-energy radiation. The above estimates do not take into account this effect. Detailed radiative-transfer calculations (as in Fig. 5) are needed to get accurate results.

A crude estimate for the high-energy luminosity generated at large radii may be obtained as follows. The rate of energy injection into the nonthermal cascade is given by equation (9). This energy is deposited to radiation via inverse Compton scattering. At small radii, the injected nonthermal power is reprocessed by the cascade to smaller photon energies E for which $\tau_{\gamma\gamma}(E) < 1$. As a result, the escaping nonthermal luminosity at energies $\sim E$, $dL_{\text{nth}}/d\ln E$, is roughly equal to the nonthermal power injected at radii $\sim R_{\gamma\gamma}(E)$,

$$\frac{1}{L} \frac{dL_{\text{nth}}}{d\ln E} \sim \frac{1}{16} \frac{\Gamma}{\Gamma_n} \frac{R_n}{R_{\gamma\gamma}(E)}. \quad (50)$$

This gives

$$\frac{1}{L} \frac{dL_{\text{nth}}}{d\ln E} \sim \frac{m_e}{16m_p} \frac{\sigma}{\sigma_{\gamma\gamma}} \frac{L_n}{L} \frac{\bar{E}_0}{m_e c^2} \frac{\Gamma^{2-\beta}}{\Gamma_n^4} \left(\frac{E}{2\Gamma m_e c^2} \right)^{1+\beta}. \quad (51)$$

This estimate suggests that at high energies, where $\gamma\text{-}\gamma$ absorption is important, the photon spectrum $d\dot{N}/dE$ can steepen from the slope β to slope $\beta - 1$.

5.4 Pure thermal Comptonization by Coulomb-heated electrons

Some GRB jets may have the ratio Γ/Γ_n near unity. Then nuclear collisions are not energetic enough to produce pions and the injection of relativistic e^\pm pairs may not occur. The proton component can still be significantly heated by (elastic) $n\text{-}p$ collisions or other processes, e.g. internal shocks, and the electron component is heated by Coulomb collisions with protons. The electron heating

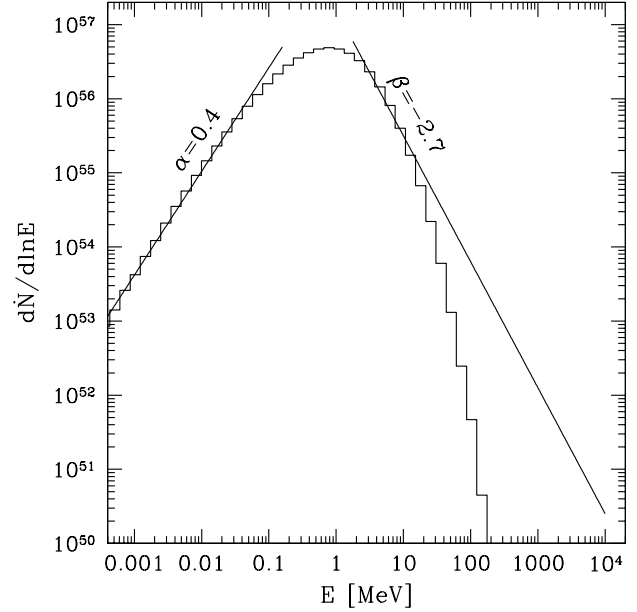


Figure 6. Photon spectrum emitted by a jet with mildly relativistic internal motions, which do not lead to pion production. Protons have a mildly relativistic temperature in the sub-photospheric region and electrons are heated only by Coulomb collisions with protons (see text).

rate \dot{Q}_{th} is proportional to the optical depth τ_T and can be significant below the photosphere. Radiation in such jets experiences pure thermal Comptonization, as the scattering electrons have a Maxwellian distribution with temperature $T_e > T_C$ (Section 4.4).

Consider a jet with mildly relativistic protons; they heat the electrons according to equation (29).¹² The resulting radiation spectrum is shown in Figure 6. Our simulation assumed the heating rate per photon $(dE/d\ln r)_{\text{th}} = 0.08\tau_T \text{ MeV}$ and followed the evolution of radiation from radius $r = 0.05R_*$ where $\tau_T = 20$. The average photon energy $\bar{E} = 1 \text{ MeV}$ was assumed at $r = 0.05R_*$. It remained close to this value up to $r = R_*$ where the jet became transparent and released the Comptonized radiation. The emitted spectrum is suppressed exponentially above $E \gtrsim 2\Gamma kT_e \sim 20 \text{ MeV}$ where $kT_e \sim 15 \text{ keV}$ is the self-consistently calculated temperature in the main heating region. The example shown in Figure 6 assumes $\Gamma = 600$. We also ran a similar simulation for $\Gamma = 300$; it gave a similar spectrum except that the cutoff occurred at $\sim 10 \text{ MeV}$ instead of 20 MeV .

Any mechanism that keeps protons hot in the sub-photospheric region leads to similar Coulomb heating of electrons and a similar radiation spectrum. For example, protons may be heated by internal shocks in the jet. Internal shocks occur at radii $r \sim \Gamma_{\text{min}}^2 \delta r$, where δr is the scale of fluctuations and Γ_{min} is the Lorentz factor of the slower parts of the jet. The scale δr may be as small as $\sim 10^6 \text{ cm}$ (the size of the central engine) or perhaps even smaller. Then internal shocks begin at a radius

¹² Protons with a smaller, sub-relativistic temperature pass faster their energy to electrons (Spitzer 1962). Then, at large $\tau_T \gg 1$, *all* of the proton heat can be taken by the electrons. In this case, the electron heating rate simply equals the dissipation rate in the jet. We consider here the case when Coulomb collisions are slow enough to create a ‘bottleneck’ for the heat flow from protons to electrons to radiation. In this case, electron heating is controlled by the rate of Coulomb collisions.

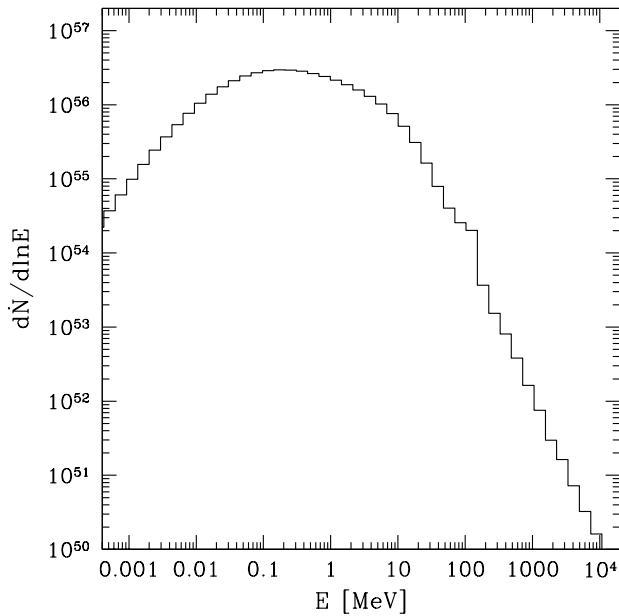


Figure 7. Photon spectrum emitted by a jet whose thermal radiation was strongly cooled before collisional re-heating. The jet has the same L , τ_0 and Γ/Γ_n as in Fig. 5, but its $\Gamma = 150$ instead of 600.

$r \sim 10^{10}(\Gamma_{\min}/100)^2(\delta r/10^6 \text{ cm}) \text{ cm}$ where the jet may have a large τ_{Γ} even without production of e^{\pm} pairs (cf. eq. 4; Γ is the Lorentz factor of the shocked part of the jet).

5.5 Strongly cooled and then re-heated radiation

The standard picture of a passively cooling jet (Section 2) predicts that radiation experiences strong adiabatic cooling before reaching R_n if $R_n \gg R_s$, which occurs for modest Γ . Thus, a regime is possible where radiation is strongly cooled before collisional re-heating.

In this case, the emitted spectrum differs from Figure 5, as illustrated by the simulation shown in Figure 7. It assumes that the jet has $\Gamma = 150$, and all other parameters are the same as in Figure 5; in particular $\Gamma/\Gamma_n = 6$, which corresponds to $\Gamma_n = 25$. The main difference caused by the smaller Γ is that the radiation temperature prior to the onset of heating drops to a low value $kT_{\min} \approx 60 \text{ eV}$ (the adiabatically cooled T_{\min} scales as $\Gamma^{8/3}$, see Section 2). It corresponds to $\bar{E}_{\min} \approx 0.025 \text{ MeV}$ and $\epsilon_{\min} \approx 6 \times 10^{-3}$ at $r \lesssim R_n$. The collisional re-heating at $r \gtrsim R_n$ is still strong in the model, giving a significant radiative efficiency $\epsilon \approx 0.4$ and a significant $\bar{E} \approx 1.5 \text{ MeV}$. The resulting spectrum has a very broad peak above $\sim 0.1 \text{ MeV}$. It is shaped by thermal Comptonization with a large Compton amplification factor $A \sim 60$. This leads to a relatively hard slope $\beta \approx -1.4$ between $E_{\text{peak}} \sim 0.2 \text{ MeV}$ and $2\Gamma kT_e \sim 10 \text{ MeV}$ where $kT_e \sim 30 \text{ keV}$ is the self-regulated temperature of the e^{\pm} plasma.

This simulation illustrates an interesting feature of Comptonization models for GRB emission. Models with efficient re-heating do not give the simple Band-type spectrum with the MeV break if the mean photon energy \bar{E} dropped much below MeV prior to re-heating. The cooling stage temporarily creates an exponential break in the radiation spectrum at a low energy $E \ll 1 \text{ MeV}$. Then re-heating and Comptonization increases \bar{E} back to $\sim \text{MeV}$; however, the recovery of \bar{E} is achieved mainly by hardening the

spectrum above the break, with only a minor shift in the break position.¹³

We conclude that a long stage of adiabatic cooling at $r > R_s$ has a significant effect on the ultimate spectrum after re-heating. In reality, this effect may never occur if the jet does not passively cool between R_s and R_n . Its proton component can be heated e.g. by internal shocks. Then Coulomb-heated electrons will keep \bar{E} and ϵ from falling, as discussed in Section 5.4. Thus, it may be that even jets with $\Gamma \sim 100 - 300$ (modest by GRB standards) keep a significant $\epsilon \gtrsim 0.1$ prior to the onset of inelastic nuclear collisions at R_n . Then their emitted spectra will be similar to the spectra of high- Γ jets shown in Figure 5.

5.6 Impact of synchrotron emission and variability on the spectrum

Two additional effects can change the observed spectra, in particular the slope α at $E < E_{\text{peak}}$:

- (i) A strong magnetic field adds synchrotron emission from e^{\pm} pairs injected by pion decay. It peaks at energies $E_s \lesssim 1 \text{ MeV}$ (eq. 18) and can dominate at $E < E_{\text{peak}}$ because the synchrotron spectrum is relatively soft, $\alpha = -1/2$.
- (ii) Variable jets consist of many thin shells with different parameters, and their radiation spectra vary on timescales as short as 10^{-4} s (in observer time). The superposition of many different instantaneous spectra is observed when the true instantaneous spectrum is not time-resolved. This tends to reduce the observed α .

Models with synchrotron emission and variability will be published elsewhere.

6 DISCUSSION

6.1 Formation of GRB spectrum

Formation of GRB spectrum is a long-standing problem. Much of the previous work focused on the optically thin internal-shock model (see Bosnjak, Daigne & Dubus 2009 for recent detailed calculations). The model posits that the observed γ -rays are nonthermal synchrotron emission from electrons accelerated at the shock fronts, and introduces phenomenological parameters of this process. Some key issues remained, however, unsettled. Why is the nonthermal electron heating efficient? Why do the reported spectra of GRBs usually peak near MeV? Why are the low-energy slopes of some GRB spectra so hard ($\alpha \gtrsim 0$, significantly harder than e.g. synchrotron emission)? As a possible solution, it was hypothesized that GRB spectra include a bright photospheric component which results from strong sub-photospheric heating (e.g. Rees & Mészáros 2005).

The results of the present paper suggest that the dominant component of GRB radiation comes from the photosphere. Collisional heating naturally gives the photospheric emission a Band-type spectrum (e.g. Fig. 5) without invoking unknown parameters apart from the Lorentz factors and the initial radius of the jet r_0 . No fine-tuning of these parameters is required to produce the typical observed GRB spectrum. The radiative efficiency of collisional

¹³ This is a robust result of unsaturated Comptonization in a relativistically expanding jet. Saturated Comptonization ($y \gg 1$) would strongly shift the peak of the spectrum, however it appears to be not relevant to GRBs as it would require photon starvation while realistic GRB jets must advect a large number of thermal photons from the central engine.

heating is large: it converts $\gtrsim 30$ per cent of the jet energy to escaping radiation.

In general, collisional heating depends on internal motions in the jet. One can imagine three possible regimes:

(A) The jet is steady (no fluctuations in Lorentz factor) and $\Gamma < \Gamma_{\text{crit}}$ (no neutron decoupling). Suppose also that there is no magnetic dissipation. Then the outflowing plasma passively cools and emits the quasi-thermal spectrum shown in Figure 1.

(B) There are moderate fluctuations $\delta\Gamma/\Gamma < 1$. Then the proton component of the jet is heated by internal shocks and nuclear collisions between protons and migrating neutrons. Electrons are heated by Coulomb collisions with protons, with a well defined rate (eq. 29). The radiative efficiency of such jets is large if the protons are hot at radii $r \sim 0.1R_*$ — then Coulomb collisions pass a large fraction of proton energy to electrons, and hence to radiation. The radiation spectrum emitted by jets with Coulomb-heated electrons is shown in Figure 6.

(C) If there are strong fluctuations $\delta\Gamma/\Gamma > 1$ or the jet has a very high Lorentz factor $\Gamma > \Gamma_{\text{crit}}$, then compound flows form with $\Gamma/\Gamma_n \gg 1$. Nuclear collisions in such jets create pions, which leads to injection of e^\pm pairs with energies $\sim m_\pi c^2 \approx 140$ MeV. The photospheric radius in this regime is regulated by the created e^\pm pairs. The electron distribution function has an extended non-thermal tail, whose shape is determined by the radiative cooling of e^\pm (Fig. 4). The jet emits the radiation spectrum shown in Figure 5. The spectrum extends to very high energies with a slope $\beta \sim -2.5$ and has an annihilation line at $\sim \Gamma$ MeV whose amplitude is sensitive to Γ_n .

Comparison of these theoretical expectations with available data suggests that GRB jets are mainly in regime C (and may be in regime B in some bursts). The impact of collisional heating on the plasma and radiation components of the jet is significant in this regime. The jet remains forever dominated by e^\pm , $n_\pm \sim 20n$. The produced radiation remains embedded in the jet until it expands to $r \sim 10^{16}$ cm. Any additional heating processes occur in the radiation field already changed by the collisional heating.

The numerical simulations in this paper were performed for weakly magnetized jets, $\epsilon_B \ll 1$, where Compton cooling dominates over synchrotron cooling. Jets with large ϵ_B are expected to have the same photospheric luminosity, with a similar spectrum that peaks near 1 MeV but has a smaller low-energy slope α . Numerical models for strongly magnetized jets will be published elsewhere.

We showed numerical examples for a typical GRB jet with isotropic equivalent of kinetic luminosity $L = 10^{52}$ erg/s. In our fiducial model we found $R_n \sim 10^{11}$ cm, $R_* \sim 10^{12}$ cm and $R_{\gamma\gamma}(E) \sim 10^{13}(E/10 \text{ GeV})^{1.5}$ cm. The model can be scaled to GRBs with different L . Jets with fixed Lorentz factors (e.g. $\Gamma = 600$ and $\Gamma_n = 100$) and fixed L_n/L will have $R_n \propto R_* \propto R_{\gamma\gamma} \propto L$, i.e. the characteristic radii will linearly scale with luminosity L . The brightest observed GRBs have $L \sim 10^{54}$ erg/s, which leads to $R_n \sim 10^{13}$ cm, $R_* \sim 10^{14}$ cm, and $R_{\gamma\gamma}(E) \sim 10^{15}(E/10 \text{ GeV})^{1.5}$ cm. In spite of this big change, the spectrum of produced radiation will be similar to that in Figure 5, because the ratios R_*/R_n and $R_{\gamma\gamma}/R_n$ are important for the spectrum formation, not the values of radii.¹⁴ The value of E_{peak} is likely to increase with L (cf. eq. 39).

¹⁴ The radius of collisional heating is limited by neutron decay at $r \sim R_\beta = 3 \times 10^{15}(\Gamma_n/100)$ cm, which does not scale with L . For the brightest jets, the radius of $\gamma\gamma$ transparency at 10 – 100 GeV becomes comparable to R_β , which could affect the spectrum shape at the high-energy end.

The slope α of the emitted spectrum is limited by the transfer effects discussed in Section 2. The hardest slope found in our radiative transfer models near 10 keV is about 0.4 (for comparison, a Planck spectrum would have $\alpha = 1$). Practically all observed GRBs satisfy this limit (e.g. Preece et al. 2000). However, larger α were reported for a few bursts (Crider et al. 1997; Ghirlanda, Celotti & Ghisellini 2003; Ryde et al. 2006). This suggests that in some bursts the jet may be inhomogeneous on tiny angular scales $\delta\theta < 1/\Gamma$.

The relativistic jet is causally disconnected on scales $\delta r > r/\Gamma^2$, and different shells δr can have different radiative history, with different R_n and R_* . Observed GRB light-curves show strong variability in a broad range of time-scales beginning from 0.1 ms. The existence of very fast variability is naturally accommodated by our model. The shortest timescale of the photospheric emission is $\delta t_{\text{var}} \sim \Gamma^{-2}(R_*/c) \sim 10^{-4}(\Gamma/600)^{-2}R_{*,12}$ s.

Note that observations of multi-GeV photons should not be used to constrain the radius of prompt emission R_{MeV} as done in Abdo et al. (2009a). They derive a minimum Γ and a minimum R_{MeV} in GRB 080916C assuming that R_{MeV} is the same as R_{GeV} (for which $\gamma\gamma$ transparency requires a large value). In fact, MeV photons should not be assumed to come from the same radius as GeV photons, even when the light-curves in the two bands are strongly correlated. The general point is illustrated by the concrete model in the present paper. The same plasma shell that emits MeV radiation at R_* can emit GeV photons when the shell expands to a larger radius $R_{\gamma\gamma}$ (Section 5.3). The temporal correlation between MeV and GeV emission is preserved, as photons emitted at different radii by the relativistically moving shell arrive to observer almost simultaneously. There is only a slight delay of the very-high-energy component emitted at $R_{\gamma\gamma}$. This delay equals the observed time of the shell expansion from R_* to $R_{\gamma\gamma}(E)$, which is $R_{\gamma\gamma}/2\Gamma^2 c \lesssim 1$ s.

Similarly, observations of optical radiation that comes from a large radius R_O and is correlated with the prompt γ -rays (Racusin et al. 2008) cannot be used to constrain the radius of the prompt γ -ray emission (see also the end of Section 6.3 below).

6.2 Internal-shock heating

The jet can be heated in the sub-photospheric region by multiple internal shocks as well as by nuclear collisions. A mildly relativistic shock front heats protons to a mildly relativistic temperature and electrons to an ultra-relativistic temperature if they receive a fraction $\epsilon_e \gg m_e/m_p$ of the dissipated energy. At the shock front, the electrons acquire a mean Lorentz factor $\gamma_{\text{inj}} \sim \epsilon_e m_p/m_e$. The details of this collisionless process are complicated and can be studied by numerical simulations (e.g. Sironi & Spitkovsky 2009). The simulations suggest that shocks in a plasma with transverse magnetic field $\epsilon_B > 10^{-3}$ produce a rather narrow (quasi-Maxwellian) distribution around γ_{inj} .

The volume-averaged e^\pm distribution function that results from shock heating is similar to that shown in Figure 4. The impulsive heating of electrons to $\gamma \sim \gamma_{\text{inj}}$ is similar to the injection of e^\pm by nuclear collisions, even though it is concentrated at the propagating shock front rather than distributed in volume. The heated electrons are quickly cooled behind the shock front and create an e^\pm cascade.

As a result, the effect of internal-shock heating on radiation is in many respects similar to that of collisional heating, and the simulations in the present paper are useful for understanding this effect. If $\epsilon_e > 10^{-2}$, γ_{inj} exceeds 20. In the sub-photospheric region,

where compactness $l \gg 10$, the shape of e^\pm distribution function at $\gamma > 20$ is not important for Comptonization as the inverse-Compton emission from these electrons is anyway absorbed by the γ - γ reaction. The shape of e^\pm distribution is quite universal in weakly magnetized jets – it is controlled by the development of e^\pm cascade in the same way for collisional heating and shock heating.

The thermal part of e^\pm distribution function must be nearly the same in the two cases. It is regulated by the heat supply from protons via Coulomb collisions and does not depend on what heats the protons – internal shocks or nuclear collisions. Therefore, Θ_e is given by equation (32) in either case.

The main difference between the nuclear collisional heating and shock heating is in the rate of electron energy injection. First note that the electron energy budget in shock heating is proportional to ϵ_e . A small $\epsilon_e \ll 1$ implies that the normalization of the relativistic tail in the averaged e^\pm distribution function is small compared to that produced by nuclear collisions, and its contribution to Comptonization is smaller. Second, the dependence of shock heating on radius is uncertain as it depends on the uncertain variability pattern of the central engine. Collisional dissipation has a special feature: the ‘nonthermal’ heating (injection of e^\pm by nuclear collisions) $dQ_{\text{nth}}/d \ln r \propto r^{-1}$ scales with r in the same way as the ‘thermal’ (Coulomb) heating $dQ_{\text{th}}/d \ln r$ (Section 4), and their constant ratio w is comparable to unity. By contrast, the effective $w(r)$ for shock heating may vary, leading to a different radiative-transfer solution for the Comptonized spectrum.

Collisional heating alone gives a ‘minimal’ emission model. Shocks and magnetic dissipation are the usual candidates for additional electron heating, which may create additional components of GRB radiation; another mechanism for collisionless heating at large radii is outlined in Section 6.3 below. If the nonthermal electron population extends to $\gamma \gg 100$, the relative contribution of synchrotron emission increases, as Compton losses are suppressed by the Klein-Nishina reduction in scattering cross-section. We did not simulate this situation here, and it can be done in the future. The general setup of radiative-transfer calculations in this paper and the developed numerical code can be used for a broad class of emission models – any combination of thermal heating and relativistic electron/positron injection in the expanding jet with any magnetization.

6.3 Heating by neutron decay

Neutrons carried by GRB jets eventually decay. Their large Lorentz factor implies a long decay time $\Gamma_n t_\beta$ where $t_\beta \approx 900$ s. The mean radius of β -decay is

$$R_\beta = ct_\beta \Gamma_n \approx 3 \times 10^{15} \left(\frac{\Gamma_n}{100} \right) \text{ cm.} \quad (52)$$

The decay occurring inside the jet has a drag effect on the faster proton component and reduces its Lorentz factor (Rossi, Beloborodov & Rees 2006). In essence, the decay injects relatively slow protons that are picked up by the jet with the relative Lorentz factor $\Gamma_{\text{rel}} = (1/2)(\Gamma/\Gamma_n + \Gamma_n/\Gamma)$. This can be described as inelastic sharing of radial momentum between the fast jet and the decaying slow neutrons, which decelerates and heats the jet. The dissipation efficiency of this process can exceed 100 per cent as the jet tends to use the heat to regain its Lorentz factor via adiabatic cooling and re-dissipate the energy.

Most of neutrons decay near the radius R_β . However, a fraction r/R_β decays at smaller radii $r < R_\beta$. Dissipation of ~ 100 per cent of the jet energy begins at radius $R_1 \sim (\Gamma_n/\Gamma)R_\beta$. Between R_1 and R_β , the jet decelerates in the background of decay-

ing neutrons in a self-similar regime (resembling the deceleration of adiabatic blast waves), and its Lorentz factor decreases as $r^{-1/2}$. This strong dissipation may generate radiation.

Note that the decaying neutrons create a perfect maser. The new protons injected by β -decay appear in the plasma frame with momentum antiparallel to the flow direction and perpendicular to the magnetic field. They immediately begin to gyrate with Lorentz factor Γ_{rel} and form a ring in the momentum space. This ring is a maser that amplifies low-frequency cyclotron waves in the plasma. The maser instability develops on a short timescale proportional to ω_B^{-1} where $\omega_B = eB/m_e c$ (e.g. Hoshino & Arons 1991). Damping of the excited waves heats the plasma. The waves may also accelerate particles. Extremely relativistic ion rings were previously studied near the termination shocks of pulsar winds and proposed to accelerate leptons (Hoshino et al. 1992). A similar heating is observed in the interaction of comets with the solar wind. In this case, a compound flow is formed as the neutral gas around the comet penetrates the solar wind; ionization of the neutral particles effectively injects charges that move with a suprathermal velocity relative to the wind plasma and immediately begin Larmor rotation.

The β -decay and maser instability produce strong volume heating between R_1 and R_β . Coincidentally, at comparable radii, optical radiation can be released as self-absorption ceases in the optical band. Besides, the jet becomes transparent to very high-energy photons. Thus, interesting radiative signatures may be expected. The radiative efficiency is, however, uncertain and likely smaller than the photospheric $\epsilon_\star \sim 0.3 - 0.5$. The emission will occur in the optically thin regime and can be of the type modeled by Stern & Poutanen (2004) and recently by Vurm & Poutanen (2009). The study of possible radiative signatures of neutron decay between R_1 and R_β is deferred to a future work.

One feature of emission powered by neutron decay can be predicted. The emission will arrive to distant observers with a slight delay with respect to the photospheric emission produced by the same neutrons via the collisional mechanism at $r \lesssim R_\star$. As the jet expands from R_\star to $r \gg R_\star$, a neutron with Lorentz factor Γ_n shifts with respect to the plasma jet a radial distance $\Delta r \approx (r - R_\star)(\Gamma_n^{-2} - \Gamma^{-2})/2 \approx r/2\Gamma_n^2$, which corresponds to observed delay

$$\begin{aligned} \Delta t_{\text{obs}} &\approx (1+z) \frac{r}{2\Gamma_n^2 c} \approx \frac{(1+z)t_\beta}{2\Gamma} \left(\frac{r}{R_1} \right) \\ &\approx \frac{(1+z)}{2} \left(\frac{\Gamma}{900} \right)^{-1} \left(\frac{r}{R_1} \right) \text{ s.} \end{aligned} \quad (53)$$

This neutron-drift delay appears to be consistent with the detected delay $\Delta t_{\text{obs}} \sim 2$ s of the prompt optical emission with respect to the main GRB pulses in the ‘naked-eye’ GRB 080319B (Beskin et al. 2009).

The delay of the GeV source detected by *Fermi* can have a similar, geometrical reason: if it operates at radii much larger than the source of MeV emission, its emission must be delayed.

ACKNOWLEDGMENTS

I grateful to I. Vurm, E. Derishev and the referee for comments that helped improve the manuscript.

REFERENCES

Abdo A. A. et al., 2009a, *Science*, 323, 1688

- Abdo A. A. et al., 2009b, *ApJ*, 706, L138
 Amsler C. et al., *Physics Lett. B* 667, 1 (2008)
 Asano K., Terasawa T., 2009, *ApJ*, 705, 1714
 Bahcall J. N., Mészáros P., 2000, *Phys. Rev. Lett.*, 85, 1362
 Band D. L. et al., 2009, *ApJ*, 701, 1673
 Beloborodov A. M., 2000, *ApJ*, 539, L25
 Beloborodov A. M., 2003, *ApJ*, 588, 931
 Beloborodov A. M., 2008, *AIP Conf. Proc.*, 1054, 51
 Beskin G. et al., 2009, submitted to *Science* (arXiv:0905.4431)
 Bosnjak Z., Daigne F., Dubus G. 2009, *A&A*, in press (arXiv:0811.2956)
 Breakstone A. et al., 1984, *Phys. Rev. D*, 30, 528
 Crider A. et al., 1997, *ApJ*, 479, L39
 Daigne F., Mochkovitch R., 2002, *MNRAS*, 336, 127
 Derishev E. V., Kocharovskiy V. V., Kocharovskiy V. I., 1999a, *ApJ*, 521, 640
 Derishev E. V., Kocharovskiy V. V., Kocharovskiy V. I., 1999b, *A&A*, 345, L51
 Fukuda S. et al., 2002, *ApJ*, 578, 317
 Fuller G. M., Pruet J., Abazajian K., 2000, *Phys. Rev. Lett.*, 85, 2673
 Ghisellini G., Celotti A., 1999, *ApJ*, 511, L93
 Ghirlanda G., Celotti A., Ghisellini G., 2003, *A&A*, 406, 879
 Ghisellini G., Ghirlanda G., Nava L., Celotti A., 2009, *MNRAS*, in press (arXiv:0910.2459)
 Giannios D., Spruit H. C., 2007, *A&A*, 469, 1
 Hoshino M., Arons J., 1991, *Phys. Fluids*, B, 3, 818
 Hoshino M., Arons J., Gallant Y. A., Langdon A. B., 1992, *ApJ*, 390, 454
 Ioka K., Murase K., Toma K., Nagataki S., Nakamura T., 2007, 670, L77
 Koers H. B. J., Giannios D., 2007, *A&A*, 471, 395
 Kumar P., Barniol Duran R., 2009, *MNRAS*, 400, L75
 Lemoine M., 2002, *A&A*, 390, L31
 Levinson A., Eichler D., 2003, *ApJ*, 594, L19
 Lightman A. P., Zdziarski A., 1987, *ApJ*, 319, 643
 Mészáros P., Rees M. J., 2000, *ApJ*, 541, L5
 Metzger B. D., Thompson T. A., Quataert, E., 2008, *ApJ*, 676, 1130
 Paczyński B., 1990, *ApJ*, 363, 218
 Pe'er A., Mészáros P., Rees M. J., 2005, *ApJ*, 635, 476
 Preece R. D. et al., 2002, *ApJS*, 126, 19
 Pruet J., Woosley S. E., Hoffman R. D., 2003, *ApJ*, 586, 1254
 Racusin J. L. et al., 2008, *Nature*, 455, 183
 Rees M. J., Mészáros P., 2005, *ApJ*, 628, 847
 Rossi E. M., Beloborodov A. M., Rees M. J., 2006, *MNRAS*, 369, 1797
 Ryde F., 2005, *ApJ*, 625, L95
 Ryde F. et al., 2006, *ApJ*, 652, 1400
 Ryde F. et al., 2010, *ApJ*, 709, L172
 Sironi L., Spitkovsky A., 2009, *ApJ*, 698, 1523
 Spitzer L., 1956, *Physics of Fully Ionized Gases* (New York: Interscience)
 Stern B. E., Poutanen J., 2004, *MNRAS*, 352, 35
 Svensson R., 1987, *MNRAS*, 227, 403
 Thompson C., 1994, *MNRAS*, 270, 480
 Vurm I., Poutanen J., 2009, *ApJ*, 698, 293

APPENDIX A: ELECTRON-POSITRON CASCADE

The compactness parameter l is large in the sub-photospheric region $r < R_*$ where most of collisional heating takes place (Section 4). It implies fast Compton cooling of e^\pm and quick γ - γ absorption of energetic photons. Therefore, the timescale for the cascade development following the injection of an electron (or positron) with $\gamma_0 \sim m_\pi/m_e$ is short compared with the jet expansion timescale. Then the distribution function of nonthermal e^\pm , $dn_\pm/d\gamma$, is locally (at a given r) quasi-steady and satisfies the equation

$$\frac{d}{d\gamma} \left(\frac{dn_\pm}{d\gamma} \dot{\gamma} \right) = S(\gamma), \quad (\text{A1})$$

where $S(\gamma) = d\dot{n}_\pm/d\gamma$ is the creation rate of secondary e^\pm , and $m_e c^2 \dot{\gamma}(\gamma)$ is the energy loss rate of electron (or positron) with a Lorentz

factor γ . The energy loss is due to Compton scattering, synchrotron emission, and Coulomb collisions with thermal electrons and positrons.¹⁵ Coulomb collisions dominate at small $\gamma \approx 1$ (and lead to quick thermalization of non-relativistic e^\pm). In this Appendix, we focus on the relativistic tail of the e^\pm distribution, where Coulomb collisions are negligible compared with Compton and synchrotron losses. Then,

$$m_e c^2 \dot{\gamma} \approx -\frac{4}{3} \sigma_T c (U_{\text{KN}} + U_B)(\gamma^2 - 1), \quad (\text{A2})$$

where $U_{\text{KN}}(\gamma)$ is the energy density of photons with energy $E' \lesssim m_e c^2/\gamma$, i.e. below the Klein-Nishina cutoff in the scattering cross section.

The source function $S(\gamma)$ may be written as

$$S(\gamma) = g(\gamma) \mathcal{M}_0 \dot{n}, \quad \mathcal{M}_0 = \frac{f_\pm \Gamma_{\text{rel}} m_p}{\gamma_0 m_e}. \quad (\text{A3})$$

Here \dot{n} is the rate of nuclear collisions in the compound flow (eq. 7), and \mathcal{M}_0 is the multiplicity of primary e^\pm injected with Lorentz factor γ_0 following a nuclear collision. Then $g(\gamma)$ is a dimensionless function that represents the source of secondary e^\pm created by one primary e^- or e^+ . This function is calculated numerically using Monte-Carlo simulations of the cascade.

Integration of equation (A1) yields

$$\frac{d\tau_{\text{nth}}}{d\gamma} \equiv \frac{\sigma_T r}{\Gamma} \frac{dn_\pm}{d\gamma} = \frac{3}{8} \mathcal{M}_0 \tau_n \frac{n m_e c^2}{U_{\text{KN}} + U_B} \frac{G(\gamma)}{\gamma^2 - 1}, \quad (\text{A4})$$

$$G(\gamma) \equiv \int_\gamma^{\gamma_0} g(\gamma') d\gamma'. \quad (\text{A5})$$

When $U_B \ll U_\gamma$, this equation becomes

$$\frac{\sigma_T r}{\Gamma} \frac{dn_\pm}{d\gamma} = \frac{3}{8} \mathcal{M}_0 \tau_n \frac{n}{n_\gamma} \frac{G(\gamma)}{\bar{\epsilon}(\gamma)(\gamma^2 - 1)}, \quad (\text{A6})$$

where $n_\gamma/n \sim 10^5$ is the photon-to-baryon ratio (the main parameter of the GRB jet, see eq. 2), and $\bar{\epsilon}(\gamma) \equiv U_{\text{KN}}/n_\gamma m_e c^2$ represents the mean dimensionless energy per photon below the Klein-Nishina cutoff. The typical $\bar{\epsilon}$ in the calculated models is near 3×10^{-3} and varies slowly with γ . The dimensionless function $G(\gamma)$ equals the number of secondary e^\pm injected with Lorentz factor above a given γ in the e^\pm cascade triggered by one primary particle. In particular, $G(1) = \mathcal{M}_s$ is the total number of secondary e^\pm . The function $G(\gamma)$ decreases from $G(1) = \mathcal{M}_s$ to $G(\gamma) \sim 1$ at $\gamma \lesssim \gamma_0$, which implies a relatively slow dependence on γ , with the average slope $d \ln G/d \ln \gamma \approx -\ln \mathcal{M}_s / \ln \gamma_0 \approx -0.7$. Then equation (A6) implies that the optical depth of the nonthermal e^\pm population τ_{nth} sharply peaks at $\gamma \sim 1$. Its value is small, $\tau_{\text{nth}} \ll 1$ (and much smaller than the optical depth of the thermalized e^\pm). However, the effect of nonthermal population on radiation is measured not by τ_{nth} , but by the Compton amplification factor $A = \int \gamma^2 d\tau_{\text{nth}}$. The amplification factor peaks at large γ ,

$$\frac{dA}{d \ln \gamma} = \frac{3}{8} \mathcal{M}_0 \tau_n \frac{n}{n_\gamma} \frac{\gamma G(\gamma)}{\bar{\epsilon}(\gamma)}, \quad (\text{A7})$$

Particles with $\gamma^2 \bar{\epsilon} \gg 1$ generate photons that are absorbed by the $\gamma - \gamma$ reaction. As a result, in the main heating region $r < R_*$, particles with $\gamma \gtrsim 20$ contribute to the development of the e^\pm cascade, while particles with $\gamma \lesssim 20$ shape the scattered radiation spectrum.

APPENDIX B: NUMERICAL CODE

The code is designed to simulate the self-consistent evolution of the radiation field and the e^\pm plasma in the jet. For collisionally heated jets considered in this paper, the following quantities are known at all radii: the injection rate of primary e^\pm with $\gamma_0 \sim 300$ (eq. 7) and the corresponding energy injection rate (eq. 9), the density of the accumulated thermalized e^\pm

¹⁵ We neglect in this paper the possibility of energy exchange between thermal plasma and nonthermal e^\pm due to collective processes.

component (eq. 24) and the heating rate of this component (eq. 29). The code aims to find the temperature of the thermalized e^\pm population $T_e(r)$, the nonthermal tail of e^\pm distribution, and the radiation field at all radii.

The calculation is split into two parts: (i) global radiative transfer in a jet with a given e^\pm distribution function, and (ii) calculation of e^\pm distribution function for a given radiation field. The consistency between parts (i) and (ii) is reached via iterations as explained below. Note that part (i) is a global problem, while part (ii) is local and can be solved separately at all radii. Temperature T_e and the nonthermal tail of e^\pm distribution at a given r are determined by the local radiation field, Coulomb heating rate, and e^\pm injection rate.

Radiation has a Planck spectrum at early stages of jet expansion (i.e. at small radii), with the temperature determined by the initial size of the jet and its energy. In the simulations, the initial thermal radiation is sampled by a large number of Planck photons ($\sim 10^9$), which are injected at a small radius and their scattering is followed until the photons escape. The code can also simulate the injection of synchrotron photons and follow them together with the Planck photons. In this paper, only weakly magnetized simulations are presented, where Compton scattering is the dominant mechanism of spectrum formation, and synchrotron emission is neglected. Before the jet expands to transparency, the photons are multiply scattered and may be absorbed by the γ - γ reaction. In each scattering event, the scattering electron is randomly drawn from the local e^\pm distribution function, and the exact Compton cross section is used to randomly perform the scattering.

The radiative transfer is calculated in the static lab frame, assuming that the plasma flows in the radial direction with a bulk Lorentz factor Γ . Since Γ is large ($10^2 - 10^3$ in the simulations) essentially all photons flow outward, and most of them have tiny angles $\theta \sim \Gamma^{-1}$ with respect to the radial direction. The radiation is essentially comoving with the plasma flow. Therefore, one can view the transfer as the evolution of radiation in time $t = r/c$ — time and radius are almost equivalent choices for the independent variable in the problem. Between successive scatterings at radii r_1 and r_2 , the photon propagates along a straight line in the lab frame, and its angle with respect to the local direction of the radial jet, θ , changes: $\sin \theta_2 = (r_1/r_2) \sin \theta_1$. This change automatically (and exactly) describes the adiabatic cooling of radiation in the opaque zone.¹⁶

When solving the radiative transfer with a trial $T_e(r)$, we find the energy gained by radiation (per photon) from scattering on thermal e^\pm . This is done by defining a radial grid r_i and accumulating statistics of scattering in each bin $\Delta \ln r$ during the Monte-Carlo simulation of the radiative transfer. Thus, we evaluate $(d\bar{E}/d \ln r)_{\text{th}}(r)$ for our trial model. If it exceeds the required $(d\bar{E}/d \ln r)_{\text{th}}$ (given in eq. 40) we reduce $T_e(r)$ in the next iteration.

The nonthermal tail is given by equation (A1), which contains the source function $S(\gamma)$ with shape $g(\gamma)$ (eq. A3). We find $g(\gamma)$ numerically using the Monte-Carlo simulation of the cascade in the local radiation field (which is known after calculating the radiative transfer in the previous iteration). The distribution of nonthermal e^\pm at small γ is affected by Coulomb collisions with the thermalized e^\pm population. This effect is included by adding the Coulomb losses to $\dot{\gamma}$ in equation (A1). The losses are evaluated approximately by assuming a cold e^\pm background;¹⁷ they are given by

equation (27) (Coulomb losses are similar for energetic protons and e^\pm). The updated nonthermal tail and $T_e(r)$ are used in the calculation of radiative transfer in the next iteration. 5-10 iterations are usually sufficient to accurately find the self-consistent solution for the radiative transfer and the e^\pm distribution function.

The iterative method also allows the code to achieve a self-consistent treatment of γ - γ absorption, which is a nonlinear effect. When the code solves radiative transfer, the opacity to γ - γ absorption $\kappa_{\gamma\gamma}$ is evaluated using the radiation field saved from the previous iteration (or an initial guess, for the first trial). In each radial bin $\Delta \ln r$, the radiation field is saved on a grid in the (θ, E) -space as a collection of $n_\theta \times n_E$ ‘monochromatic beams’. The γ - γ opacity seen by a given photon with energy E_0 propagating at angle θ_0 is calculated by integrating over all target ‘beams’ $(\Delta\theta, \Delta E)$ (with a random azimuthal angle) that are above the threshold for reaction $\gamma + \gamma \rightarrow e^+ + e^-$. As the photon (E_0, θ_0) traverses the radial bin $\Delta \ln r$, the probability of its survival is $\exp(-\kappa_{\gamma\gamma} \Delta r / \cos \theta_0)$.

¹⁶ This can be understood by considering the toy problem of coherent and isotropic scattering in a cold jet. Then a scattering event does not change the photon energy in the local plasma frame E' ; it only changes its angle. Between successive scatterings, the energy of the freely propagating photon in the lab frame $E = \text{const}$, and $E' = E\Gamma(1 - \beta \cos \theta)$ is decreasing because of decreasing θ . In addition, the propagating photon becomes preferentially beamed outward in the plasma frame (θ' decreases). Next scattering again randomizes $\cos \theta'$ and destroys the preferential beaming, suddenly increasing (on average) θ' . As a result, the next scattering on average reduces the photon energy $E = E'\Gamma(1 + \beta \cos \theta')$ in the lab frame.

¹⁷ The exact shape of the e^\pm distribution function in the region connecting the thermal and nonthermal parts requires the full treatment of Coulomb collisions with a finite-temperature plasma. However, this region radiates very little, and the approximate matching of the thermal and nonthermal components (as in Fig. 4) is sufficient for the radiative transfer simulations.